2009

Characterization of gaseous oxygen and methane injectors under high pressure combustion

Ryan Saffell

CHARACTERIZATION OF GASEOUS OXYGEN AND METHANE INJECTORS UNDER HIGH PRESSURE COMBUSTION

by

RYAN SAFFELL

A THESIS

Submitted in partial fulfillment of the requirements
for the degree of Master of Science in Engineering
in
The Department of Mechanical and Aerospace Engineering
to
The School of Graduate Studies
of
The University of Alabama in Huntsville

HUNTSVILLE, ALABAMA

2009

In presenting this thesis in partial fulfillment of the requirements for a master's degree from The University of Alabama in Huntsville, I agree that the Library of this University shall make it freely available for inspection. I further agree that permission for extensive copying for scholarly purposes may be granted by my advisor or, in his/her absence, by the Chair of the Department or the Dean of the School of Graduate Studies. It is also understood that due recognition shall be given to me and to The University of Alabama in Huntsville in any scholarly use which may be made of any material in this thesis.

Ryan J. Saffell

3/11/09
(date)

THESIS APPROVAL FORM

Submitted by Ryan J. Saffell in partial fulfillment of the requirements for the degree of Master of Science in Engineering in Mechanical Engineering and accepted on behalf of the Faculty of the School of Graduate Studies by the thesis committee.

We, the undersigned members of the Graduate Faculty of The University of Alabama in Huntsville, certify that we have advised and/or supervised the candidate of the work described in this thesis. We further certify that we have reviewed the thesis manuscript and approve it in partial fulfillment of the requirements for the degree of Master of Science in Engineering in Mechanical Engineering.

Marlow D Moser 11 Mar 2009 Committee Chair
Dr. Marlow D. Moser (Date)

Robert A Frederick 3/12/2009
Dr. Robert A. Frederick, Jr. (Date)

Kader Frendi 3/11/09
Dr. Kader Frendi (Date)

Kader Frendi 3/11/09 Department Chair
Dr. Kader Frendi (Date)

Phillip A Farrington 3/13/09 College Dean
Dr. Phillip Farrington (Date)

Debra M. Moriarty 5/1/09 Graduate Dean
Dr. Debra M. Moriarity (Date)

ABSTRACT
School of Graduate Studies
The University of Alabama in Huntsville

Degree Master of Science in Engineering College/Dept. Engineering/Mechanical and Aerospace Engineering

Name of Candidate Ryan J. Saffell

Title Characterization of Gaseous Oxygen and Methane Injectors under High Pressure Combustion

A program to examine and characterize two types of coaxial injectors and two types of screw swirl injectors in a small-scale rocket engine using gaseous oxygen and gaseous methane as main propellants has been developed. The mixing efficiency of this gas-gas scheme was evaluated by measuring the combustion efficiency at various characteristic chamber lengths, which allowed assessment of combustion stability of the system, and by changing parameters such as chamber pressure, mixture ratio, and injector post recess. Combustion efficiency for the shear coaxial element increased about 5% with chamber pressure and oxygen post recess. The shear coaxial injector combustion efficiency also increased about 15% from the shortest chamber length examined to the longest. Swirl coaxial and screw swirl performance increased about 7% with decreasing chamber length. The swirl coaxial element was more effective at mixing than the others and performance decrease was primarily due to heat loss. The screw swirl injector followed the same trends as the swirl coaxial injector.

Abstract Approval: Committee Chair Marlon D Moss

Department Chair [signature]

Graduate Dean Debra M. Moriarty

ACKNOWLEDGMENTS

I would like to thank everyone at the Propulsion Research Center who has helped me with this project. First, thanks to Dr. Marlow Moser for advising me and allowing me to work on this project, as well as helping me to make some sense out of it. Thanks to Mr. Tony Hall for his expertise, teaching, and guidance during my time as an undergraduate intern and through graduate school. Dr. Dave Lineberry was a constant source of knowledge and I would like to thank him for allowing me to annoy him with all of my questions. To the undergraduates, Adam Tuck, Bryant Swanner, and Max Franks, I am very appreciative for their efforts during the sweltering heat of an Alabama summer. Thanks to everyone else for helping me to keep most of my sanity.

I am forever grateful for the late Dr. Clark Hawk. He offered me a summer internship without ever meeting me and after only one letter of correspondence. He also provided me a way to come to graduate school with a research assistantship. He was always teaching me and keeping me on my toes, making sure I knew what I was doing. I will forever remember his graciousness and fun-loving attitude.

TABLE OF CONTENTS

LIST OF FIGURES

Figure **Page**

LIST OF TABLES

Table **Page**

LIST OF SYMBOLS

A	Area
α	Conversion factor, thermal expansion coefficient
c^*	Characteristic velocity
c_p	Specific heat
D	Diameter
f_{TR}	Nozzle throat influence factor
γ	Specific heat ratio
L	Chamber length
L^*	Characteristic chamber length
$\dot{m}$	Mass flow rate
MW	Molecular weight
N	Number of injector elements
η_{c^*}	Characteristic velocity efficiency, combustion efficiency
P	Pressure
R_G	Outside radius of chamber
R_O	Inner radius of chamber
Ru	Universal gas constant
ρ	Density
S	Swirl number
T	Temperature
t	Time
U, u	Axial velocity
V	Volume
w	Circumferential velocity

Subscripts

a	Annulus
avg	Average

C	Chamber
con	Contraction of nozzle
Cu	Copper
f	Fuel, flame
i	Inner
in	Inlet
o	Outer, stagnation
ox	Oxygen
prod	Products
R	Ratio, reference
rel	Relative
t	Throat
th	Theoretical
vc	Vortex chamber

NOMENCLATURE

CFD	Computational Fluid Dyanamics
DNS	Direct Numerical Simulation
ERE	Energy Release Efficiency
GOX	Gaseous Oxygen
LES	Large Eddy Simulation
LIF	Laser Induced Florescence
LDV	Laser Doppler Velocimetry
LOX	Liquid Oxygen
OFHC	Oxygen-Free High Conductivity
PDPA	Phase Doppler Particle Analyzer
PLIF	Planar Laser Induced Florescence
PIV	Particle Imaging Velocimetry
PLC	Programmable Logic Controller
PRC	Propulsion Research Center
PROPEP	Propellant Formulation Characterization Program
RANS	Reynolds-Averaged Navier Stokes
TEP	Thermal Equilibrium Program
UAH	University of Alabama in Huntsville

CHAPTER 1

INTRODUCTION

Injectors are the sole means of providing and mixing propellants in a rocket engine. They come in different geometries, operations, and applications, but serve the same purpose: to mix propellants in such a way as to aid combustion. The engine will then transfer the thermal energy from combustion into kinetic energy to propel the rocket. This is not unlike the internal combustion engine of an automobile. The fuel injector of a car injects a fine mist, or highly atomized spray, into the cylinder where it mixes with air. The atomization helps the liquid to evaporate. The piston then compresses and a spark ignites the mixture to provide power to the vehicle. A similar action is performed inside of a rocket engine, except without a piston to increase pressure. Multiple types of injectors exist and are industrially used today: shear, swirl, impinging, showerhead, and pintle are just a few.

Characterization of how injectors perform has taken many forms throughout history. Different types of tests are used to visualize and describe the behavior of a certain injector or group of injectors. These include cold-flow testing, where pictures can be taken of the flow and propellant mixing can be measured. Also, hot-fire testing can

provide performance information, as well as combustion behavior due to the injector design. Linking these two models can be used to fully characterize a rocket injector.

1.1 Historical Background

Rocket injectors come as varied as the engines that use them. There are many different types of injectors that have been and are currently used in engine systems. Depending on the specifications of a particular engine and operation, a certain injector is chosen. Design of an injector is based on these specifications, which can be different per injector type.

1.1.1 Injector Types

Injectors are an essential component of rocket engines and fall into two general groups, impingement or shearing, which are differentiated by their mixing mechanics. Design variables for each type differ, such as size and operation, but some always overlap, including propellant flow rates and stability concerns. All types of injectors work by mixing fuel and oxidizer in order to combust, as shown in a common schematic of injector components and a rocket engine, Figure 1.1. The combustion inside the engine or chamber is essentially a large diffusion flame. The flame is characterized by a holding point, flame shape and size, and flame surface, where the propellants burn at an equivalence ratio of one.[1] The injector type can determine where the flame is held, such that damage to the injector faceplate or chamber can be minimized. Injector flames are typically treated as turbulent diffusion flames when trying to express their behavior.[1,2,3] While this description is generally uniform for rocket engines, the injector design for causing combustion is quite varied.

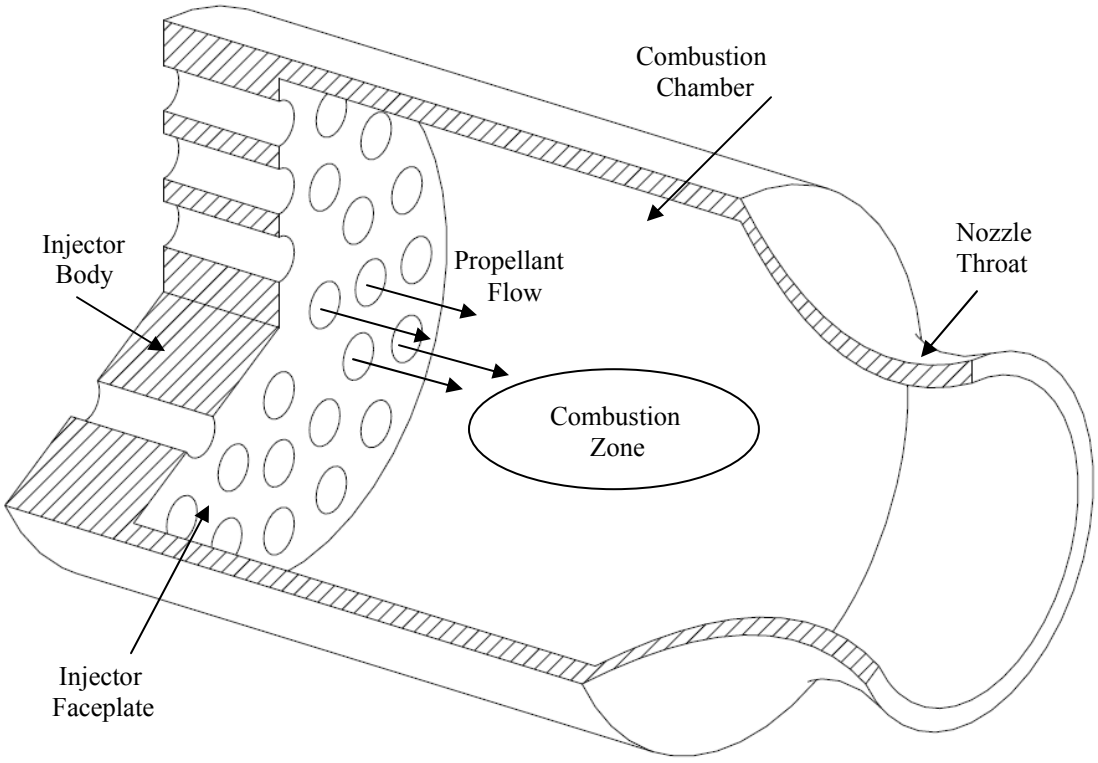

Figure 1.1 Relation of injector components to engine

Impinging injectors are typically composed of two or more streams of two or more propellants flowing into the combustion chamber at a designated angle to the injection faceplate. At some specified distance away, the streams collide, or impinge, with one another, mix, atomize, and burn. Figure 1.2 shows schematics of different impinging types. The design parameters of impinging injector elements depend on, but are not limited to, impingement angle, fuel and oxidizer spacing, and propellant impingement (like-on-like or like-on-unlike). Advantages of impinging injectors are their high mixing efficiency and atomization capability and performance record. Disadvantages include difficult manufacturing and poor throttling performance.[4] Uses of

impinging designs include heavy-lift engines such as the F-1 and H-1, Titan boosters, and the Lunar Excursion Module ascent stage, among others.[4]

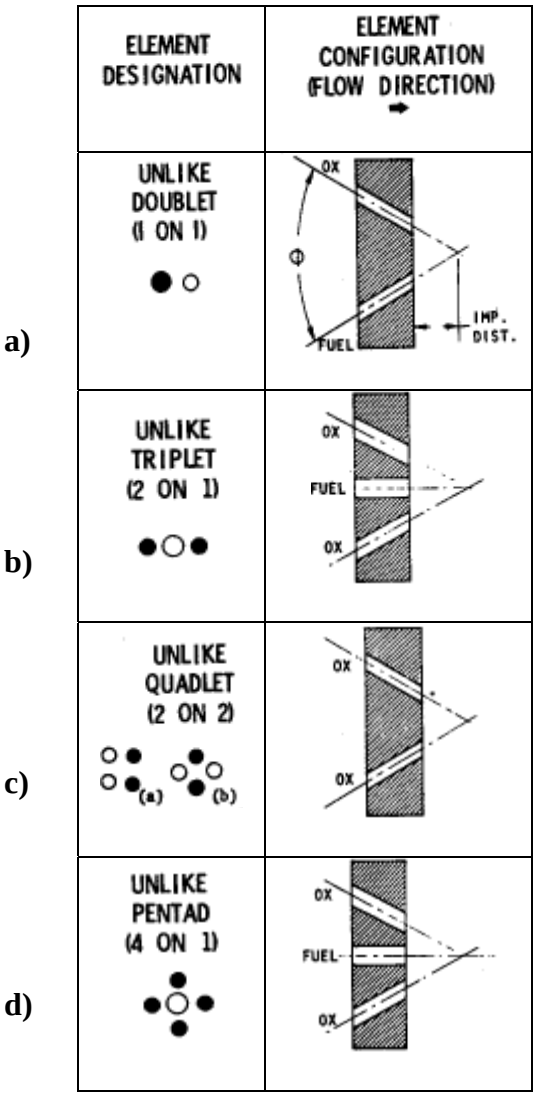

Figure 1.2 Impinging injectors schematics[4]

Other impinging types can be generalized to include splash plate injectors and pintles. Splash plate injectors involve separate jets of fuel and oxidizer colliding on a plate, triggering high atomization and mixing. This element type was employed on the Apollo Command Module for reaction control as well as other small thrusters because of its throttling capability and dependability.[4] However, wall compatibility with the propellants and combustion effects were a concern, as could be expected. Pintle injectors utilized a translatable piston to control propellant mass flow. This aspect provided simplicity and great throttling, which made it ideal for the Lunar Excursion Module descent engine. But, volatility of the hydrazine propellant raised wall compatibility concerns.[4]

Shearing injectors are generally those that do not have impingement, depending on the shearing action between two flows. These typically involve concentric tubes, one smaller than the other, or one single tube. Element types include shear coaxial, swirl coaxial, screw swirl, premixed, or showerhead. In general, one propellant flows down the smaller central tube while another propellant flows along the outside tube, concentrically, and begins mixing at a specified point close to the injector outlet. Mixing can, and generally does, continue downstream, even to the nozzle throat.

With shear coaxial injectors, propellants mix in a shearing layer formed between two concentric propellant streams. Generally, the outer propellant stream flows at a faster velocity, causing it to tear the inner propellant away from its stream. This forms a mixing layer between the two jets where atomization occurs and combustion can take place. Figure 1.3a shows a schematic of a shear coaxial injector, which is relatively simple in design and operation. The shear coaxial element provides easy manufacturing

and low pressure drop, which benefits the propellant supply system, but poor mixing and throttling. Uses for this injector type have been quite extensive in Russia and U.S., such the J-2, RL-10, and Space Shuttle engines.[4]

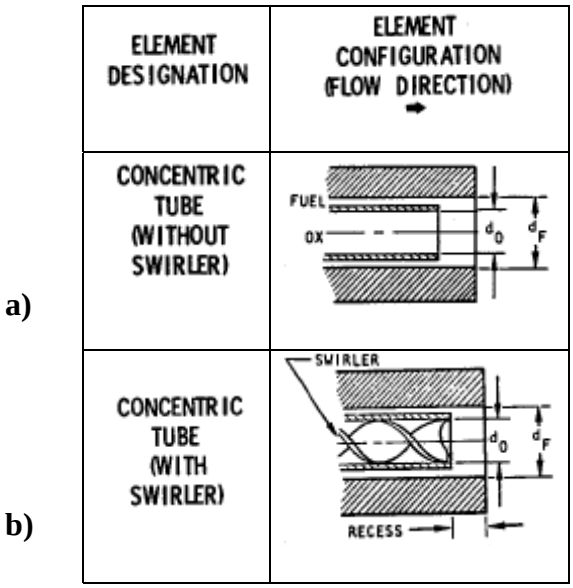

Figure 1.3 Coaxial injectors schematics[4]

Swirl coaxial elements work almost in the same manner. The exception is that either one or both of the propellant streams are swirled, typically by tangential inlets into the injector tube. This swirling action forces the propellants to form sheets (if the propellants are liquid) that exit the injector at an angle, which is referred to as the spray angle. Figure 1.3b shows this injector schematic. The secondary, or outer, flow can help or hinder mixing, depending on the design and propellants, but swirl coaxial elements have generally the same benefits as the shear injector. The swirling action makes propellants self-atomizing, which increase mixing and atomization.[5] While being heavily studied in the U.S.,[6,7,8] the this injector type has been employed mostly by Russian

engines like the RD-57 and RD-170, for example.[9,10] Screw swirl injectors behave similarly to swirl coaxial, but are swirled due to angled channels machined into the injector. This injector type has only recently been developed and experimentally studied.[11] Figure 1.4 presents a sample screw swirl element. An alternate version of the screw swirl type is the cross flow injector. While using angled channels, the propellants cross inside the injector body. This causes higher turbulence of each propellant stream, some premixing, and ultimately more efficient mixing.

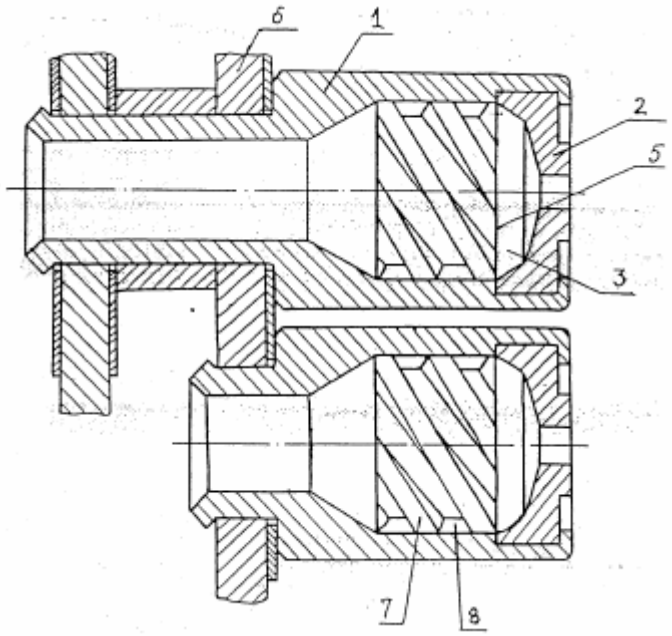

Figure 1.4 Sample screw swirl injector schematic[5]

A premixed injector mixes propellants before entering the combustion chamber, then injects the mixture down a single tube or orifice, but can produce one major problem. Premixing the fuel and oxidizer can cause a combustible mixture inside the

injector body. If the flame in the combustion chamber were to travel upstream into the injector, which has a much smaller area than the chamber, could lead to injector burning and damage or even a catastrophic explosion in the injection bulkhead. Premixed injector types are thusly not generally employed in rocket engines.

Showerhead injectors are also very simple in design. Propellants stream from individual tubes and mix in the chamber, downstream of the injector face. This type was used in one the first rockets ever produced, the German V-2, but has not been utilized since[12] due to its poor mixing. The showerhead injector requires a large chamber volume for good combustion, making it heavy and costly.

There are many variations of both main categories of injectors. There are many advantages and disadvantages to either injector type and have been used in rocket engines according to their specific design criteria. But, both shearing types and impinging types undergo the same design criteria and preliminary testing.

1.1.2 Injector Design

Design of rocket injectors has as long of a history as rocket engines. Today, computer codes handle most of the mathematics involved in designing an injector. Given the operational specifications and perhaps a desirable injector type, the code can output dimensions and other parameters so the injector can be made. These rely on the basic formulations for rocket engine operations[12] and other derived correlations. For example, in Reference 13, the Rupe mixing criterion[14] was used to assist in the design of some elements. Individual designers and companies also have their own correlations and means for determining injector parameters. The Aerojet Company developed the platelet design[15] in the mid-1960s for different types of injectors. They modify this legacy design

for different applications based on their design methods. On the other hand, Bazarov developed design criteria and correlations for swirl injectors.[16] This method uses desired pressure drop across the injector plus propellant and operational specifications to output dimensions of an individual swirl element or multiple elements.

These correlations and computer codes are a quick and cheap method to obtain injector parameters. They, of course, have been supported by experimental data, which often require a not so quick and cheap design method, trial-and-error. This method may produce the most ideal or exact design of an element, but requires costly and time consuming testing. The computer codes and correlations are probably the most efficient means to design a rocket injector.

1.2 Common Testing Methods

Injector characterization not only involves design of the injector, but also physical and numerical testing. Design can only give a prediction of how the injector should perform. To actually know and understand how it operates in real life and real-time conditions requires physical hardware testing. This testing can then be used to validate and support the design. Three main types of testing are cold-flow, hot-fire, and Computational Fluid Dynamics (CFD). Each type provides different details of the injector performance.

Cold-flow testing uses propellant simulants, such as water or water solution, if the operating propellant is toxic or difficult to handle, like hydrazine. Often one propellant will be used alone or with a simulant in order to prevent combustion. For example, liquid oxygen can be used alone or with a gas simulant for the fuel, depending

on the operating condition and testing type. On the other hand, two different simulants can be used to simulate both the oxidizer and the fuel, depending on the testing type.

Cold-flow test diagnostics include shadowgraphy, Schlieren, Partical Image Velocimetry (PIV), Phase Doppler Particle Analyzer (PDPA), Laser Doppler Velocimetry (LDV), and patternators. The first two methods use a lighting technique to visualize the flow from the injector. They provide two-dimensional black and white images of the flow and yield information such as spray angle, length of the main fluid core, spray patterns, and spray instability information. They can be instantaneous or time-averaged, depending on what is needed. The PIV, PDPA, and LDV systems used non-intrusive laser techniques to measure flow properties. These methods provide detailed information of liquid droplets, such as position and velocity tracking. The equipment required for these systems can be intricate and costly, including high power lasers and sensitive cameras. Patternators use a large array of tubes to capture propellants or simulants. The mass distribution or mixture distribution can then be measured by the levels of propellants/simulants in each tube. While the cold-flow methods provide high quality information of the propellant flow, injector and engine performance can not be measured because combustion changes propellant behavior, like break up, mixing, etc.

Hot-fire testing is where combustion occurs. Since operational engines combust propellants, this testing method is most applicable to yielding accurate performance data. Testing diagnostics include performance measurement, chemiluminescence, and planar laser induced fluorescence (LIF or PLIF). One performance measurement is characteristic velocity, c^*, efficiency, which is also referred to as combustion efficiency. This is a comparison of calculated c^* versus a theoretical value. It can also be measured

using chamber pressure or thrust. Another performance test is energy release efficiency (ERE). ERE is a comparison of the combustion temperature versus a theoretical value and has been used extensively in past research.[13,17] Due to high combustion temperatures, ERE is typically calculated using a heat flux measurement through the chamber walls and a modeled theoretical temperature. But, this can be very unreliable because the actual measurement is difficult to obtain due to material incompatibility with the high temperatures. Chemiluminescence and LIF are non-intrusive techniques that measure species concentrations, specifically excited states of OH and CH. The equipment required for these testing types can be as elaborate as that used for the cold-flow testing methods above. The difficulty of the methods is the optical access inside the combustion zone because they require windows that can perturb combustion. These methods provide visual measurements of where the combustion occurs.[8]

Scaling is an important factor when testing rocket engine components. Much injector testing today exists in the form of small scale testing. This method is much cheaper to perform than full scale testing simply because hardware, propellant, facility, etc., expense is much less and can produce results more quickly. The major concern with sub-scale testing is applicability to the full scale system. There are many methods and comparisons that can be made between the different scales as outlined in Reference 16. But, some examples of various analogs that link full scale to small scale includes matching of some non-dimensional parameters such as Reynolds number, Schmidt number, Mach number, etc. Another area of concern is instability. Combustion instability is an undesirable effect in rocket engines that can lead to a myriad of problems and is designed to be as minimized. Hence, it is heavily studied and a major part of

injector design. In Reference 18, a sub-scale testing method for finding instability modes of a full-scale injector using gaseous simulants of liquid propellants is described. As these hot-fire methods provide detailed information of the combustion process, they can also be used as validation of another testing diagnostic.

CFD uses information from hot-fire and cold-flow tests to validate a physics based computer model to predict injector behavior.[2,3] These models are used in various methods, such as Reynolds-Averages Navier Stokes (RANS), Unsteady RANS, Large Eddy Simulation (LES), or Direct Numerical Simulation (DNS). With increasing mathematical complexity and decreasing investigation size, these CFD models can be either a simple and less accurate or complex and expensive means to show injector or engine behavior. They can provide very descriptive information on the flow from the injector as well as flame and combustion details, although these models tend to involve simple combustion,[2] i.e., single-step reactions and miss the detailed kinetics. While being able to do this, though, all CFD models must be validated by actual testing. Combining all of these different testing types and methods can yield a thorough and qualitative characterization of a rocket injector.

1.3 Literature Review

Three types of injectors were studied in this research: shear coaxial, swirl coaxial and cross flow. The shear coaxial element and swirl coaxial element have been heavily studied with various fuels including hydrogen,[6,7,20,21] kerosene, propane,[22] natural gas,[23] and methane.[6,8,23,24,26] The screw swirl, or cross flow, injector has only recently been studied for use in rocket engines, but the technique has been employed in various applications, such as heat exchangers and turbine blade cooling.[25] Due to such recent

interest in methane fuel for rocket engine applications,[26,27,28] gaseous methane and oxygen were used as main propellants for this research. While future missions will most likely be interested in using liquid propellants, the gaseous state provides preliminary and fundamental research. Past experimental research on the two coaxial injector types have primarily focused on propellant flow field visualization,[20,26,29,30] flame visualization,[31,32,33] stability assessment,[24,34] cold flow statistics,[26,35] and velocity and mixture ratio effects on combustion efficiency[20,29,30] at various flow regimes, i.e., sub-, trans-, or supercritical pressures.

Another factor examined in past injector research, although not as frequent as above, was chamber length,[36,37,38] which was the main diagnostic used in the present study. Trinh[36] examined c^* efficiency at two different chamber lengths, 9 and 13 inches, as well as other parameters, using an impinging-type injector; no affect of chamber length on η_{c^*} was found. Yatsuyanagi, et al.[37] determined an empirical correlation for the efficiency of the characteristic velocity, η_{c^*}, versus a non-dimensional equivalent chamber length for a subscale LOX/Hydrogen engine using a shear coaxial injector. Tamura, et al.[38] applied this correlation to a LOX/Methane combustor and compared it with findings from Reference 37. In studies performed comparing injectors, it was found that shear injectors require more chamber length to obtain equivalent mixing of swirl injectors for LOX/Methane[37] and LOX/Hydrogen.[38] Shear coaxial mixing was slower, requiring a longer chamber to achieve thorough mixing.

1.4 Objectives

The objective of this study is to obtain hot-fire performance statistics of various injector types, primarily the shear coaxial, swirl coaxial, and screw swirl elements. This

study focuses on the effect of the characteristic length, L^*, of the combustion chamber on combustion efficiency, as well as effects of oxygen-post recess, chamber pressure, velocity ratio, and mixture ratio. The L^* is a ratio of the chamber volume to the nozzle throat area and is used to compare combustors of different rocket engines. It is also a measure of residence time for propellant mixing inside a combustion chamber.[19] Studying characteristic length effects on combustor performance has various applications to rocket engines. Combustor dimensions can be more effectively designed for either small or large thrust engines, as well as for preburner applications. Another rationale for highlighting L^* effects was due to the little amount of detailed work done on this topic.

CHAPTER 2

EXPERIMENTAL APPROACH

2.1 Overview

The goal of this research is to characterize rocket injectors based on measured performance. Before experimentation was started, a literature review was conducted to provide testing phenomena that were of research interest. Previous methods of testing were reviewed and compared with the current system at the PRC. Also, historical data of various injector schemes were available for comparison with current testing. The center already had some injector elements available for study, including a shear coaxial, swirl coaxial, and one cross flow injector, so integration with test hardware was implemented and new hardware was made. The new hardware allowed for easy and quick access to install and exchange injector elements. In addition, another cross flow element was manufactured for comparison with the other injector designs. At the same time, methods to test these injectors were developed. In order to be able to characterize and understand injector performance, each injector studied was submitted to various operating conditions to explore their behavior. Critical parameters of injector operation were adjusted to study injector and engine performance. These included chamber pressure, mass flow rate, and injector and engine dimensions. Modification of these factors allowed for variation in

other performance parameters as well. Finally, validation of the results was conducted, which verified the data and procedure. This methodology provided a well rounded characterization of the three injectors.

2.2 Test Facility

The test facility provides the infrastructure of hardware and software for conducting experiments. It is divided into two regions, an indoor monitoring area and an outdoor test cell, so rocket testing can occur in a safe manner. The test cell houses most of the equipment and hardware needed for experimentation, as shown in Figure 2.1. It is separated into five areas by cement blast walls for increased safety. Two storage areas hold the propellant supply tanks, oxygen on one side, and fuel on the other. Propellants do not come into contact with each other until they reach the rocket engine, a major safety precaution. Propellant feed lines made from 316 stainless steel were plumbed from the storage tanks, through multiple control valves, and up to the rocket. Pressure settings for the feed lines were set using hand regulated valves, which set nitrogen pressure on top of a dome loader to control propellant line pressure.

Test Cell 1 houses the research rocket engine where firings occur and measurements can be taken. Each pressure and temperature channel recorded measurements at 500 Hz, taken by a 16-bit 333 ksample/s system. Chamber pressure measurement, as well as other critical pressures, was made with Sensotec transducers with a 200 Hz low-pass filter, which had a systematic uncertainty of 0.1% full scale, or 3 psi. Temperature was measured using an Omega K-Type thermocouple with a 2 Hz low-pass filter. All measurements were fed into the instrumentation room, which holds

the data acquisition hardware and timing control board. Test Cell 2 houses air-breathing experiments and other projects.

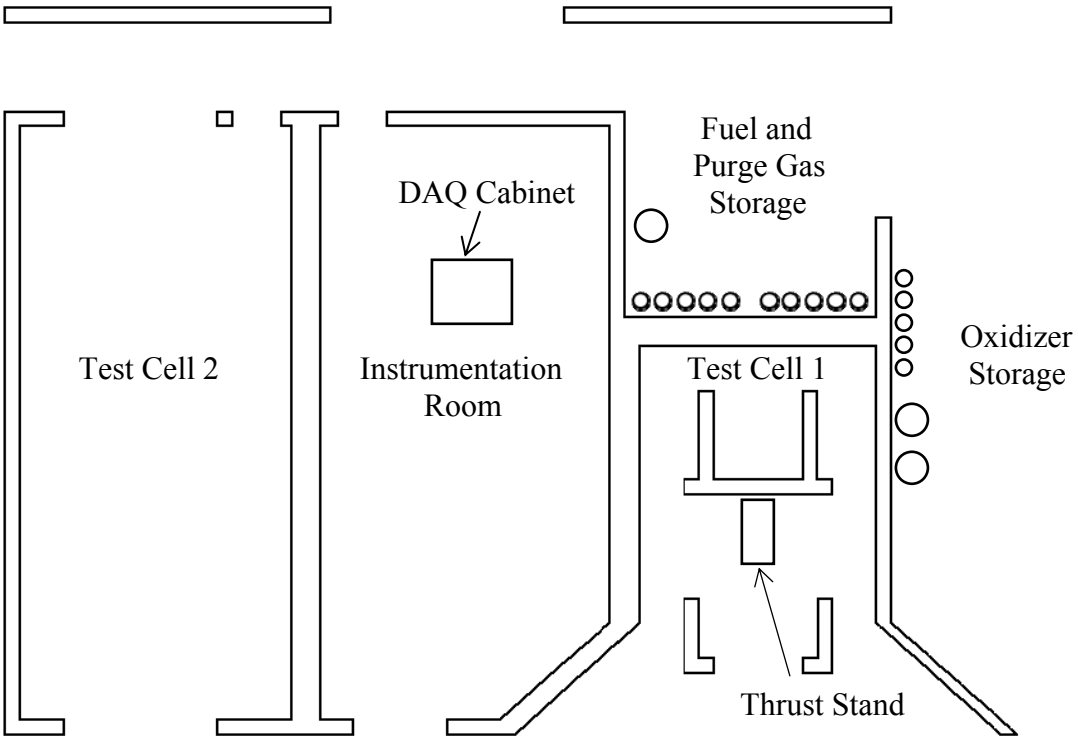

Figure 2.1 Test stand schematic

The indoor monitoring area is completely separated from the test cell, so the testing crew can be safely away from the hot-fire experiments. This area houses the security camera monitors as well as the test monitoring system. All measurement data are streamed indoors at real-time for instantaneous examination of tests. A control board operates flow valves, firing, and manual shutoff in conjunction with the automatic timing system. A computer monitors the tests while the test crew observes on closed-circuit television. This facility allows for maximum safety precautions for tests conducted.

2.2.1 Test Hardware

The main test element is a small scale research rocket engine, which is mounted on a thrust stand. The engine and stand are shown in Figure 2.2. The mounting surface was installed with flexors, so the surface was able to pivot and thrust could be measured.

Figure 2.2 Research rocket engine mounted on thrust stand

The small-scale rocket engine is a modular design, consisting of individual OFHC copper rings of different lengths held together by grade 8 steel compression rods. The copper served as a heat sink, so it could survive the high temperature tests. Different sized rings allow for finite adjustment of engine length. Engine outer diameter was five inches with an inner diameter of 2.125 inches. Additionally, acrylic rings can be installed to permit flame visualization. Since performance data were desired, chamber pressure measurement was vital. Depending on the chamber length, there were several ports available for chamber pressure measurement. Only one port was used, which was closest to the midpoint of the engine, typically at the ignition plane. The engine was ignited using a small GOX/Hydrogen torch igniter attached to the top part of the igniter section. The O_2/H_2 allowed for easy ignition versus the main propellants, O_2/CH_4, because the minimum ignition energy is much lower, $2.0*10^{-5}$ J for hydrogen and $33*10^{-5}$ J for methane.[1] The engine nozzle was also composed of OFHC copper and water-cooled so that there could be minimal time lapse between firings. A schematic of the chamber design is shown in Figure 2.3.

The combustor was configured for use of a single injector element but could be arranged for implementation of multi-element injectors. Single element injectors were installed using different mounts, specific to the injector design.

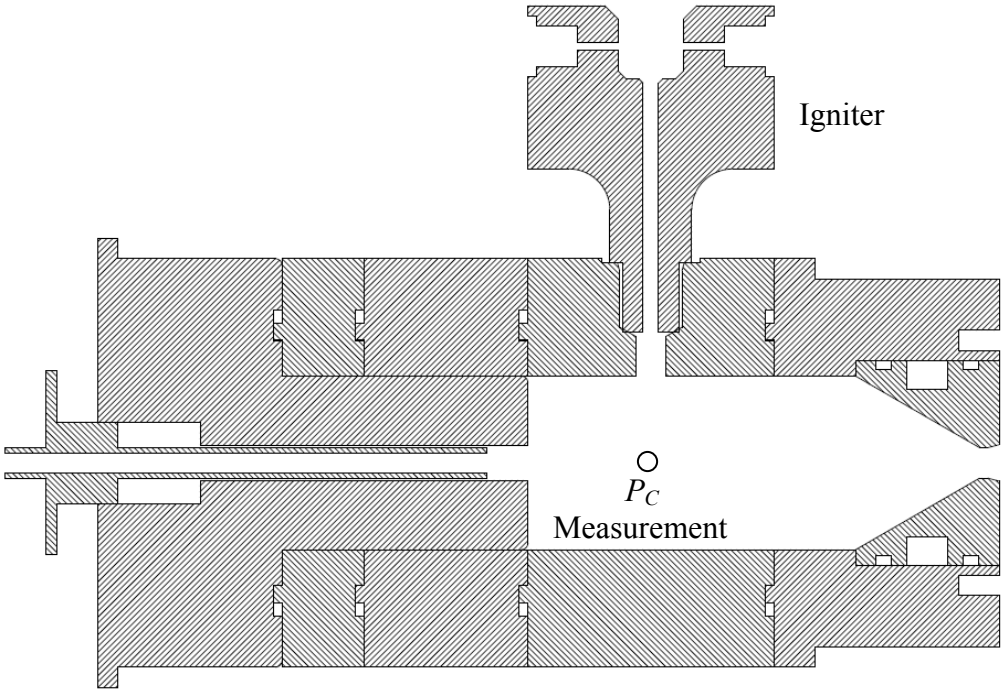

Figure 2.3 Chamber design schematic with igniter

2.2.2 Test Software

All injector tests were monitored and controlled using various software programs. Valves controlling propellant feed line paths were operated using a ladder logic program, which was controlled by two PLC program tools from Omron. The first software package, SysWin 3.2, operated during the initial shear coaxial injector tests. An upgraded version, CX-Programmer, succeeded for the remaining tests. Real-time data were streamed into a computer where it was processed using LabView 8.0. This raw data were copied into an Excel spreadsheet that handled all necessary performance and operational calculations. The theoretical c^* was calculated using Thermal Equilibrium Program, TEP. This program is based on the Gordon and McBride code, which evaluates

combustion products at equilibrium conditions by minimizing Gibbs free energy.[39] Based on propellant mixture ratio and chamber pressure, correlation curves were created for frozen and equilibrium flow.

2.2.3 Test Procedure

Test procedures were determined from the literature review, desired parameters, and previous test experience. Injector testing was divided into different periods based these parameters: injector readiness, test stand availability, and test stand and chamber readiness. Prior to any firings, step-by-step directions for conducting daily tests were made while considering all safety measures. These procedures provided detailed information for operating test equipment, gathering data, and following strict safety precautions for all personnel. These directions are presented in Appendix A. Another safety measure was to determine structure safety factors and to ensure all materials and devices were adequate for the high pressure, high temperature combustion testing. The combustion chamber was of critical importance for operational safety because of the extreme conditions. Stress analyses were performed on various parts of the chamber and it was deemed safe for all operating conditions. These calculations are provided in Appendix B.

The shear coaxial injector was first to be tested and followed a specific test matrix shown in Appendix C in accordance with injector parameters, detailed in the next section. Figure 2.4 shows schematics of two different configurations of the shear coaxial tests with variations in chamber length and oxygen post recess. Firings were set to last 4 seconds while data were collected for 10 seconds. This allowed for pre-firing measurement biases of equipment to be accounted, steady-state operation during firing,

and appreciable post-firing information of any residual effects. Valve control timings for these firings are depicted in Appendix D. All devices used for measurements during shear coaxial tests are provided in Appendix E.

Figure 2.4 Shear coaxial injector/chamber configurations.
[a) Flush injector, $L^* = 149$ in. ($L = 4$ in.); b) 0.50 in recess, $L^* = 344$ in. ($L = 10$ in.)]

The next injectors tested were the swirl coaxial and stainless steel screw swirl elements. These were designed by Dr. Vladimir Bazarov for study in the small-scale rocket engine. Testing methodology followed a similar test matrix, as shown in Appendix C. Details of differences between the two test matrices are explained in the next chapter. Test timing was the same as the shear element, shown in Appendix D.

Measurements were taken in the same manner as described previously, using the same devices as previous testing, shown in Appendix D.

After all of the above tests were completed, another chamber configuration was introduced. Based on data from some of the preceding tests, visual inspection of the flame and combustion behavior was desired. An acrylic chamber section was installed on the combustion chamber at the injection plane. This allowed for inspection of the injection and combustion phenomena into a high pressure chamber for the three surviving injectors. A high-definition camera captured this process at 1000 Hz and provided very detailed qualitative information of the flame. Multiple tests at various operating conditions for each injector were examined using the acrylic section. Details of the data gathered from these tests are presented in the next chapter. Although informative, no performance data gathered using the acrylic section were used for final injector analysis.

2.3 Test Parameters

In order to obtain performance characteristics of the four injectors – shear coaxial, swirl coaxial, and two screw swirl – various critical parameters need to be measured, calculated, and compared. First, the injector dimensions must be identified. Schematics of each injector are shown in Figure 2.5 and dimensions in Table 2.1. The shear coaxial injector is a simple design using a standard tube size and fixed annulus. A factor influencing performance of this injector type is oxygen post recess.[40] The post was recessed to three locations in relation to the injection plane: flush, 0.25 inches (one post diameter), and 0.50 inches (two post diameters). The swirl coaxial element, also referred to as the swirl nut, and the stainless steel screw swirl element were manufactured prior to testing. Post recess is also a factor of performance for this design, but was not able to be

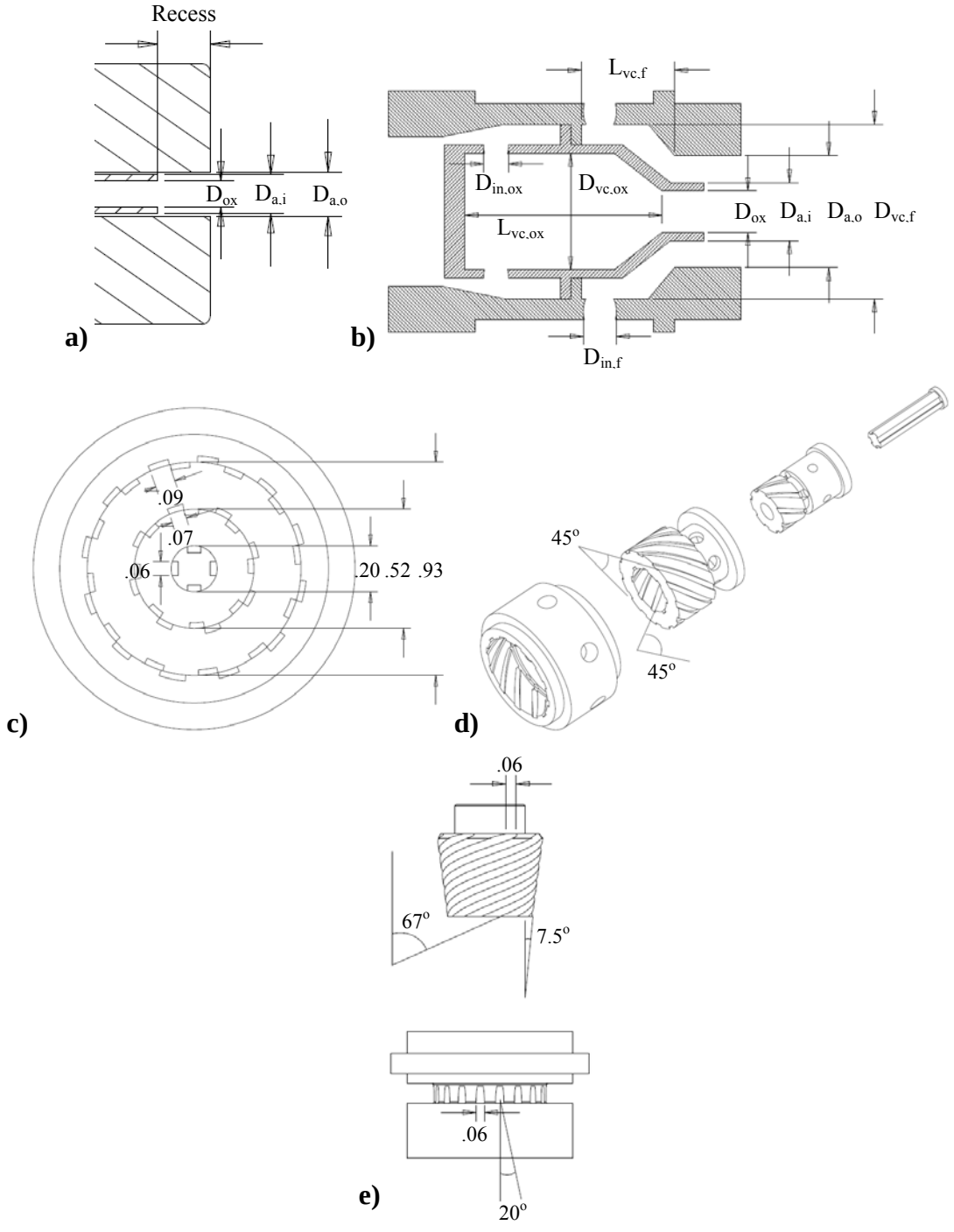

Figure 2.5 Injector schematics with critical dimensions.
[a) shear coaxial; b) swirl coaxial; c) stainless steel screw swirl fire face; d) stainless steel screw expanded view; e) copper screw swirl exploded view]

Table 2.1 Critical injector dimensions in inches.
[Cross flow injectors had multiple inlets, so effective diameter is listed]

Dimension	Shear Coaxial	Swirl Coaxial	SS Cross	Copper Cross
Recess, in	[0,0.25,0.50]	0.10	0	0
D_{ox}, in	0.247	0.10	-	-
$D_{a,i}$, in	0.321	0.14	-	-
$D_{a,o}$, in	0.34	0.27	-	-
$D_{in,ox}$, in	-	0.06	0.286	0.159
$D_{in,f}$, in	-	0.08	0.194	0.255
$D_{vc,ox}$, in	-	0.28	-	-
$D_{vc,f}$, in	-	0.42	-	-
$L_{vc,ox}$, in	-	0.47	-	-
$L_{vc,f}$, in	-	0.23	-	-
Spray Angle, degrees	-	90	90	Unknown

adjusted on the swirl nut. Based on dimensions of this element, design calculations from Reference 16 can be backed out; these are shown in Appendix F. These calculations show that the swirl coaxial element was originally designed for liquid propellants. The copper cross flow element was manufactured after testing began and was the final injector examined.

The stream and mixing pattern for both cross flow injectors are depicted in Figure 2.6. Rather than straight, uniform injection of the shear coaxial injector or circumferential swirling of the swirl nut, the stainless steel cross flow element had crossing channels such that each propellant passed each other at least twice inside the injector body. The copper cross flow injector had two different flow paths for each propellant. Oxygen was fed axially into a nut shaped like a screw, causing swirl. Methane entered through small capillaries that ran along the side of the nut with a slight angle, which caused a slight swirl effect. The propellants then exited through holes

evenly spread around the injection face and mixed, causing the more uniform flame structure.

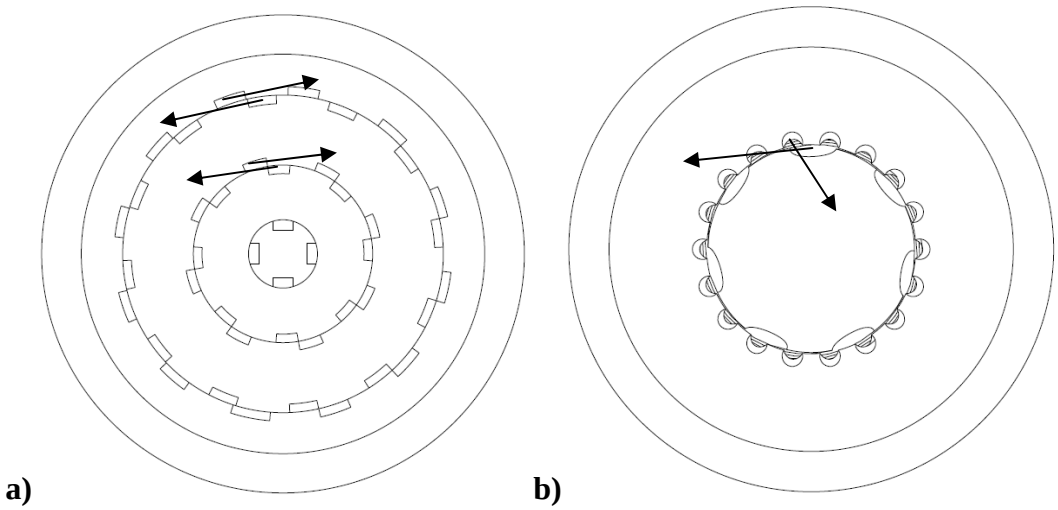

Figure 2.6 Cross flow injectors flow paths.
[a) Stainless steel injector; b) copper injector]

Combustion chamber adjustment was also a major variable and was the primary diagnostic for studying injector performance. Length was varied between 4 and 10 inches in 2 inch increments, whether with all copper rings or an acrylic section. This length adjustment altered L^*, the characteristic chamber length, which is a ratio of chamber volume to nozzle throat area, as given by Equation 2.1.

$$L^* = \frac{V_C + V_{con}}{A_t}. \tag{2.1}$$

Here, V_C is the chamber volume, V_{con} is the volume of the nozzle contraction, and A_t is the nozzle throat area. The characteristic chamber length settings were 149, 214, 279, and 344 inches.

Critical operational parameters were also varied. These include chamber pressure, propellant mass flow rate, and mixture ratio, or *O/F*, which is the ratio of oxygen mass flow rate to methane mass flow rate. Using the theoretical *c** values from TEP and the nozzle throat area, theoretical chamber pressures, P_C, were obtained using Equation 2.2.

$$P_C = \frac{\dot{m}c^*}{A_t}. \tag{2.2}$$

The total mass flow rate, $\dot{m}$, was found by summing the flow rates of oxygen and methane, which were chosen a priori. Chamber pressures were designed to be about 250 and 500 psia. Selection of *O/F* settings of 2.5 and 3.0 allowed for slight variation in each propellant flow rate, but kept the same ideal chamber pressure. These two values for mixture ratio were chosen because they straddle the peak of the specific impulse curve for methane-oxygen propulsion. Thus, high performance was expected for each setting. Combined, the mixture ratio and propellant flow rate affect velocity ratio. Using the propellant properties of specific heat ratio, γ, and molecular weight, *MW*, propellant *c** values were calculated by

$$c^* = \frac{\sqrt{\gamma \frac{Ru}{MW} T}}{\gamma \sqrt{\left(\frac{2}{\gamma+1}\right)^{\frac{\gamma+1}{\gamma-1}}}}. \tag{2.3}$$

Here, γ is the specific heat ratio and *Ru* is the universal gas constant. Temperature, *T*, was assumed to be a nominal 300 K, or 80 ^{o}F. In order to control mass flow rate, venturies were needed. Using the propellant *c** values, chamber pressures, and mass flow rates, venturi diameters were calculated using Equation 2.2 such that

$$A_{venturi} = \frac{\dot{m}_{propellant} c^*_{propellant}}{P_O}. \tag{2.4}$$

This value was used to choose a venturi of approximate area that was readily available such that the stagnation pressure was low enough for the facility to handle and high enough for the venturi to remain choked. Also calculated were feed pressure settings for each propellant. The same equation was used to calculate feed pressure because the feed tanks were assumed to be at total pressure. These procedures were done for each injector type and adjusted for their respective pressure drops. The overall nominal propellant variables are listed in Table 2.2. Details of these calculations are presented in Appendix G. Nominal bulk propellant flow velocities were 219 ft/s and 851 ft/s for oxygen and methane, respectively, for a mixture ratio of 2.5, and 230 ft/s and 745 ft/s, respectively, for a mixture ratio of 3.0.

Table 2.2 Hot-fire nominal flow conditions.
[For each *L**, the *Pc*, propellant flow rate, *O/F*, the shear oxygen post were varied]

O/F	$\dot{m}_{ox}$, lbm/s	$\dot{m}_f$, lbm/s	$\dot{m}_{total}$, lbm/sec	Nominal *Pc*, psia
2.5	0.1	0.04	0.14	250
2.5	0.2	0.08	0.28	500
3	0.105	0.035	0.14	250
3	0.21	0.07	0.28	500

Finally, performance information was calculated. The primary diagnostic of performance was combustion efficiency, as determined from *c** efficiency. This was measured as a ratio of measured *c** to theoretical *c**, Equation 2.5.

$$\eta_{C^*} = \frac{c^*_{act}}{c^*_{th}}. \tag{2.5}$$

The theoretical value was determined for each test based on the correlation found for the equilibrium assumption for nozzle flow given by TEP and measured chamber pressure and flow rates from the test. The curve fits given by TEP for a range of *O/F* is shown in Figure 2.7. Equations of these curves are stated in Equations 2.6 and 2.7.

$$c^*_{250} = 226.98(O/F)^3 - 2215.4(O/F)^2 + 6921.4(O/F) - 795.65. \tag{2.6}$$

$$c^*_{500} = 210.96(O/F)^3 - 2107.2(O/F)^2 + 6731.2(O/F) - 721.23. \tag{2.7}$$

Using these polynomials, which had less than 0.03% difference per *O/F* value, where c^*_{250} and c^*_{500} are characteristic velocity values at the nominal chamber pressures 250 psi and 500 psi, respectively, and the average chamber pressure, the test's theoretical characteristic velocity was found by interpolating between the two curves, given by Equation 2.8.

$$c^*_{th} = c^*_{500} - \frac{500 - P_{C,avg}}{250} * \left(c^*_{500} - c^*_{250}\right). \tag{2.8}$$

Here, c^*_{th} is theoretical c* and $P_{C,avg}$ is the measured average chamber pressure. The measured *c** was calculated from the average steady-state chamber pressure and the mass flow rates. The mass flow rates were calculated using Equation 2.4 with the measured average stagnation pressure, where *c** for each propellant was calculated from Equation 2.3 from measured average stagnation temperature. For these calculations, generally 500 points taken from the middle of the firing time where operation was most stable. Some deviations from this occurred for the cross flow injectors because 500 data points were not available.

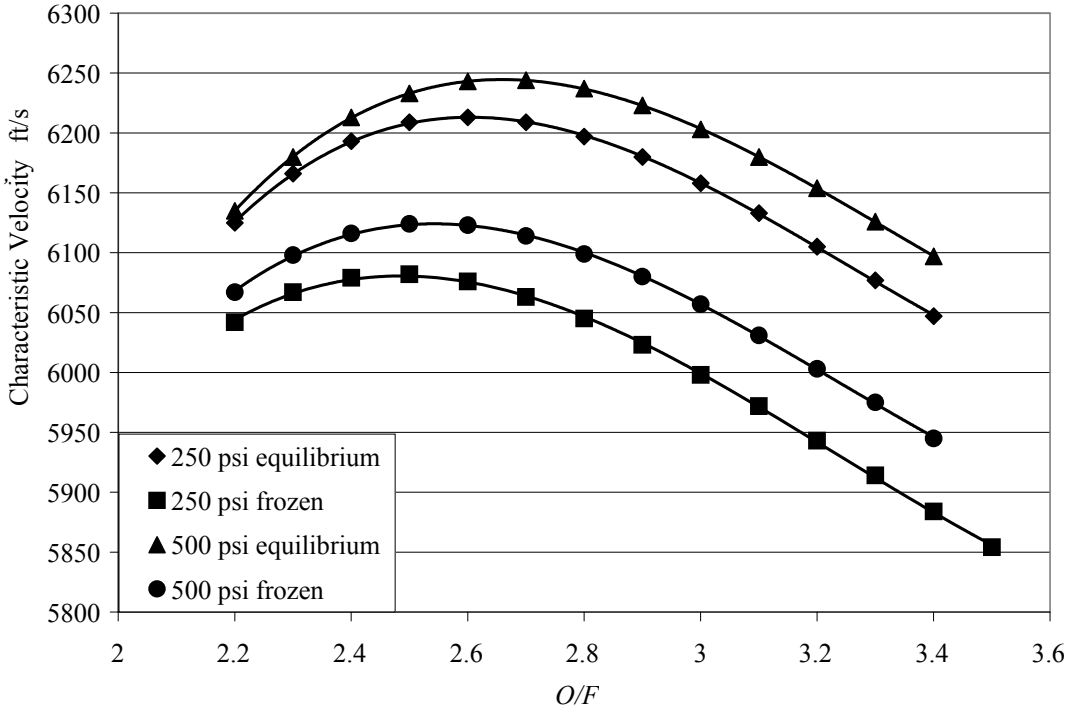

Figure 2.7 *c** curves from TEP for equilibrium and frozen flow

Another performance characteristic measured was chamber temperature. This allowed for calculation of heat flux to the chamber walls. Injectors with better performance provide more complete combustion and higher temperatures, thus larger heat flux. From the equations for energy storage and conservation of energy, a relative combustion temperature was found using Equation 2.9.

$$T_{rel} = T_f - \frac{c_{p,Cu} V_{Cu} \rho_{Cu} \Delta T}{\left(\dot{m}_{ox} + \dot{m}_f\right) c_{p,prod} \Delta t}. \tag{2.9}$$

This was compared with a theoretical flame temperature from a propellant combustion program, PROPEP, and to correct efficiency calculations.

CHAPTER 3

RESULTS

Performance results from all injector testing are presented in this chapter. The first injector tested was the shear coaxial element. This element provided baseline injector data for comparison with the other elements, as well as historical comparison. The swirl coaxial element was next tested and compared with the shear coaxial injector, as well as historical data. Testing of the stainless steel and copper cross flow injectors followed. Combustion efficiency trends of all injectors were compared. For all tests, at least two trials were run to check for repeatability and visual confirmation of the exhaust plume. For cases that showed considerable deviation between the two runs, multiple trials were performed, and then compared.

3.1 Shear Coaxial Injector

The shear coaxial injector element successfully fired 120, 4-second tests for a total of 480 seconds of hot-fire testing. Venturi sizes used in this series of testing were 0.093 inch diameter for fuel, 0.113 inch for oxygen. A photograph of a sample test firing shows the plume with the definitive blue color of methane-oxygen burning in Figure 3.1. Combustion efficiency results are presented per oxygen post recess in Figure 3.2 and relative uncertainty bars are shown in Appendix H. The legends for Figure 3.2 display

the arrangement of data: squares correspond to the 2.5 mixture ratio set point, circles correspond to 3.0; shaded symbols represent low chamber pressure and open symbols represent high chamber pressure. At a quick glance of the shear coaxial injector results in Figure 3.2, it is obvious that combustion efficiency, η_{c*}, generally increases with L^*. In addition, combustion efficiency is higher at the higher chamber pressures. Comparison between the three recess plots show that the flush oxygen post and 0.25 inch (one oxygen post diameter) recess have approximately the same efficiency values, while the 0.50 inch recess post obtained higher efficiencies. The same results were shown in Reference 40 for LOX/Hydrogen shear coaxial studies of flush and one oxygen post diameter recess.

Figure 3.1 Shear coaxial injector firing with exhaust plume

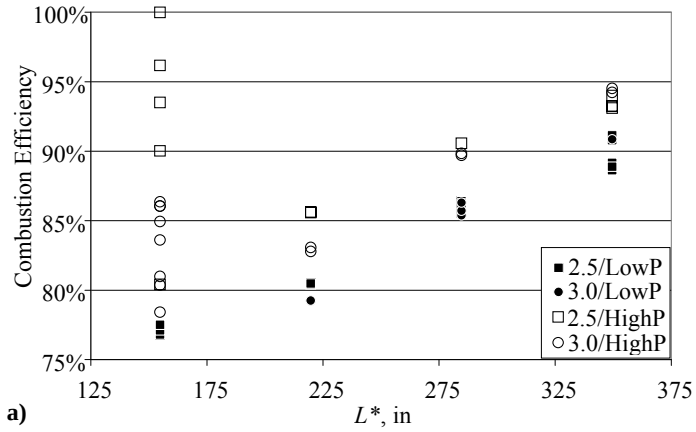

a)

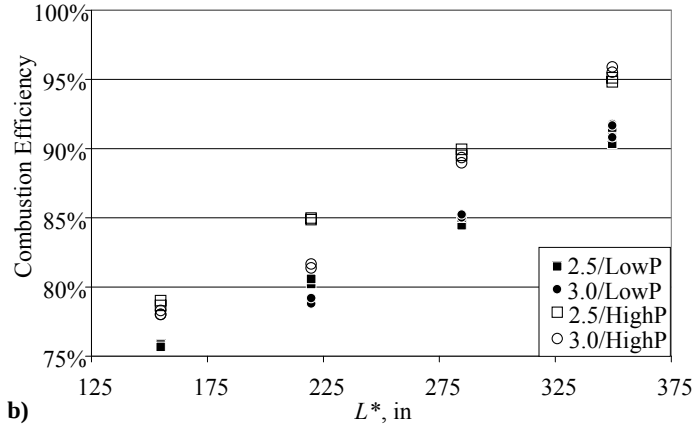

b)

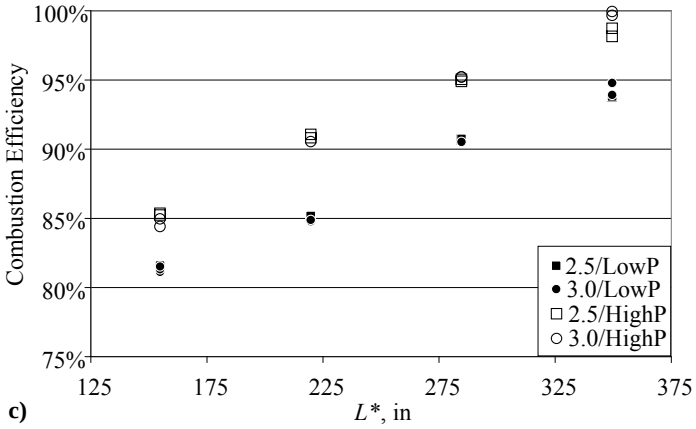

c)

Figure 3.2 Shear coaxial injector hot-fire results.
[a) Flush; b) 0.25 inch recess; c) 0.5 inch recess. Uncertainty bars shown in Appendix H]

Mixture ratio, had little to no effect on c^* efficiency, as shown in Figure 3.2 (circles and squares). This data are dissimilar to results from Trinh[36], which implemented impinging injectors, but similar to Tamura et al.[24], which used coaxial injectors, while both utilized LOX/Methane propellants in their respective small scale combustors. Since mixture ratio drives velocity ratio as discussed in the previous chapter, there was little to no effect of velocity ratio on combustion efficiency, which was also the case in Reference 24. The main difference seen in the efficiency values per L^* setting are the chamber pressure values. That is, the higher η_{c^*} values for one setting of L^* correspond to the higher chamber pressure and the lower efficiency values correspond to the lower chamber pressure.

Another important performance parameter is the injector pressure drop. This is critical because if the pressure drop is too low, coupling between any disturbances in the combustion chamber can affect upstream flow. This could lead to flow constrictions and poor performance.[41,42] It could also cause flow stoppage or reverse flow, which could lead to a pogo oscillation phenomenon. The average pressure drops per L^* setting and per post recess are listed in Table 3.1. The measured pressure drops are very low for an operational injector. A general rule-of-thumb is to have the injector operate with at least a 20% pressure drop to effectively negate the adverse effects. The simple design of this injector element did not provide a means to control pressure drop, causing the low values shown in Table 3.1. It is interesting to note the trends associated with this aspect. Pressure drop across the oxygen post increased with recess and decreased with L^*. But, the fuel pressure drop decreased with both recess and L^*. The effect of recess on oxygen and methane pressure drop was likely due to methane filling more of the recessed area

plus combustion occurring there. With the increased recess, mixing occurred slightly upstream of the injection plane in the annulus region. This contributed to the higher performance and the pressure drop variation. Pressure drop relations with chamber pressure and mixture ratio closely match those with recess and characteristic chamber length.

Table 3.1 Injector pressure drops per L^* and recess setting

L^*	Recess, in	ΔP_{ox}	Std Dev	ΔP_f	Std Dev
344	0	4.0%	0.5%	8.7%	1.4%
	0.25	4.0%	0.4%	6.5%	1.2%
	0.5	4.8%	0.3%	6.4%	1.2%
279	0	4.0%	0.3%	9.0%	1.3%
	0.25	4.3%	0.4%	8.1%	1.6%
	0.5	4.9%	0.6%	7.0%	1.5%
214	0	4.5%	0.6%	9.5%	1.4%
	0.25	4.8%	0.5%	8.8%	1.1%
	0.5	5.5%	0.5%	7.9%	1.0%
149	0	6.1%	1.0%	10.8%	1.8%
	0.25	5.8%	0.5%	9.3%	1.4%
	0.5	6.6%	0.4%	8.7%	1.1%

Most chamber/injector configurations operated steadily with no adverse symptoms. But, since acoustic/instability modes are a function of the combustion chamber and injector dimensions, one configuration showed peculiar results. The main deviation from the general trends of the shear coaxial element occurred at the shortest L^*

value for the flush (no recess) injector configuration at high pressure and mixture ratio of 2.5, test name 149/Flush/2.5/HighP. This configuration allows for the shortest distance, and thus shortest time, for propellants to mix and combust. Six trials were run at this arrangement; no two tests showed similar data. The pressure traces for these six tests are shown in Figure 3.3. Test 1 (Figure 3.3a) is the only test that displayed steady behavior, similar to all other tests performed at other chamber/injection configurations. The other five tests at this configuration have some unsteadiness prevalent in them. While Test 2 (Figure 3.3b) and Test 3 (Figure 3.3c) were rough and unsteady the entire run, Test 4 and Test 5 (Figures 3.3d and 3.3e, respectively) were constant but rough at one pressure, then dropped in pressure at some time during the test and remained steady, but not rough. Test 6 (Figure 3.3f) climbed in chamber pressure for about 90 percent of the run time then became steady for the last 10 percent. The unsteadiness observed resembles low frequency instability, but due to a 200 Hz filter on the chamber pressure transducer, this could not be confirmed. In general, when combustion is unstable, efficiency increases. Thus, this unsteady and rough behavior in Tests 3 and 6 and rough components of Tests 4 and 5 led to the higher efficiencies shown in Figure 3.2 while the constant, steady tests and components followed the general trend of lower efficiencies at the lowest L^* value.

During trials using the acrylic chamber design, attempts were made to visualize the flame behavior at this seemingly unsteady configuration. It was speculated that the flame behaved differently than at the stable arrangements. Tests were also conducted at other chamber/injector configuration to ensure combustion stability. Figure 3.4 shows pictures taken from the high-definition camera during these tests. The flame was seen to

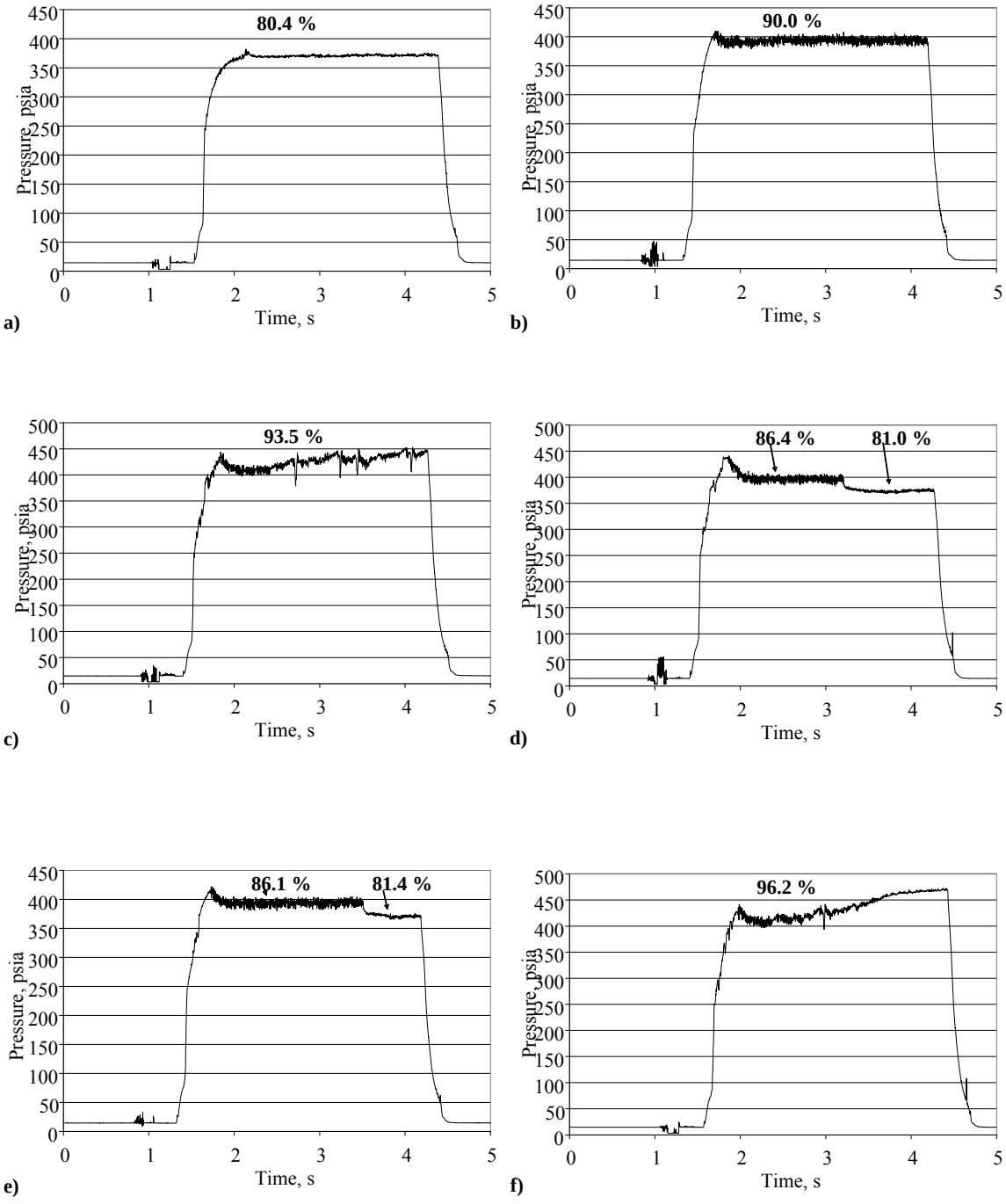

Figure 3.3 Chamber pressure traces with configuration 149/Flush/2.5/HighP.
[a) Test 149-1; b) Test 149-2; c) Test 149-3; d) Test 149-4; e) Test 149-5; f) Test 149-6. Only test 1 operated with steady behavior. Efficiency values are shown above pressure traces. Other tests at this configuration showed variable unsteadiness during firing]

hold to the injector post, as desired. The flame structure was smooth and conical, as expected. Multiple trials of test name 149/Flush/2.5/HighP were operated. While all tests conducted using the acrylic had higher performance results, no instability was captured either visually or from the pressure curves, shown in Figure 3.5. Video confirmed very smooth and uniform flame propagation from the injector face, which matched behavior at the other L^* settings, but was unexpected. This is most likely due to the different acoustic properties of copper and acrylic. The acrylic, and the rubber gasket between acrylic and copper, probably acted like a damper for the vibration from combustion and effectively killed the instability for two possible reasons. First, the additional burning contributed more fuel to the region closest to the injection plane, which is the most influential area for disrupting flame propagation. Second, the acrylic has lower thermal conductivity than copper, $0.121\frac{BTU \cdot ft}{h \cdot ft^2 \cdot °F}$ versus $226\frac{BTU \cdot ft}{h \cdot ft^2 \cdot °F}$, respectively, so the heat sink was effectively absent. This is an example of how such a small change can affect the onset of instability. As for the higher performance, this was contributed to burning of acrylic and rubber during the 3 second tests. Chamber pressures were generally higher because of the added fuel, but decreased during sequential tests, as shown in Figure 3.5. The lower melting point of acrylic, about 270^{o}F, contributed to slight erosion of the interior wall, increasing chamber volume, and causing the slight decrease of chamber pressure over sequential trials. The gaseous propellant rocket thus acted somewhat like a hybrid rocket motor. For the one acrylic section used, the post-test inner diameter of the most downstream side had expanded from 2.125 inches

a) 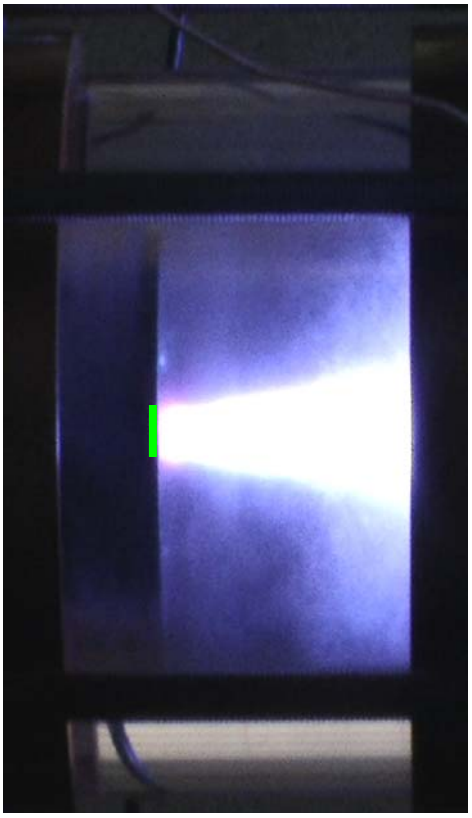

b) 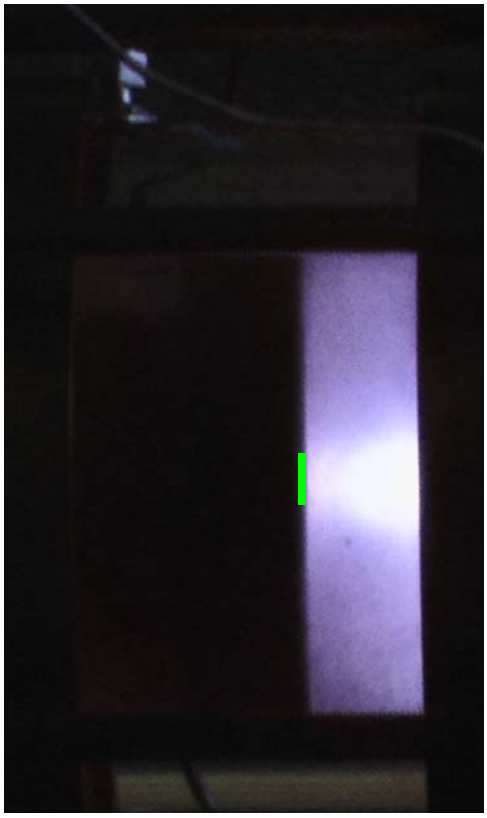

c) 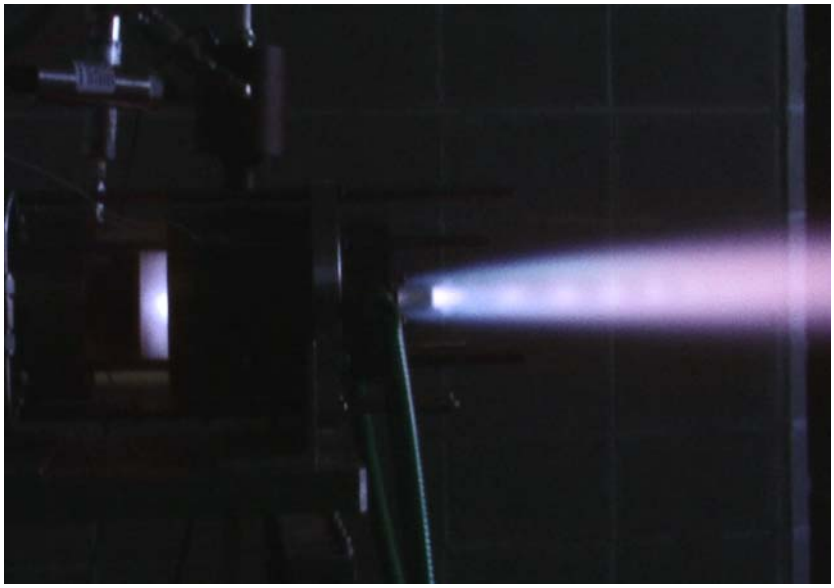

Figure 3.4 Photographs of shear coaxial injector using acrylic chamber section. [The green line marks the injector face. a) Close-up view of flame for test 279/Flush/2.5/HighP; b) Close-up view of flame for test 149/Flush/2.5/HighP; c) Full view of flame and plume for test 149/Flush/2.5/HighP]

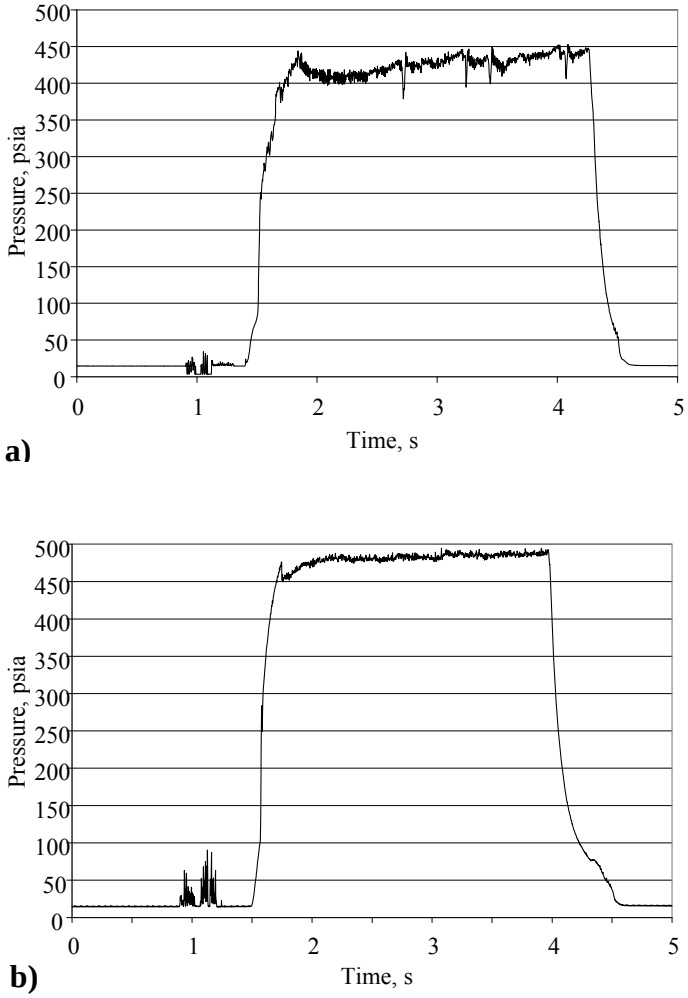

Figure 3.5 Comparison of tests at 149/Flush/2.5/HighP.
[a) Without acrylic section installed; b) With acrylic section installed]

to 2.25 inches. If erosion was assumed equal during each trial, then only approximately 0.003 lbm/s of acrylic was being added to the flow, which is only about 2 percent of the total propellant flow. Nevertheless, due to these factors, efficiency values were calculated to be between 100% and 110% for all trials, higher than nominal tests, and was

the reason they were excluded from the above analyses. Inspection of parts of the injector exposed to the flame showed no defects due to combustion.

Also assessed in this study was comparison with historical data. Previous work had been performed on chamber length studies and its effect on combustion efficiency[37,38] for LOX/Hydrogen and LOX/Methane. Instead of using the L^* value, those authors chose a non-dimensional value of chamber length, $\overline{L}_C$. This value is a ratio of chamber length to chamber diameter and calculated using Equation 3.1.

$$\overline{L}_C = \frac{L + \alpha U_R \left(\frac{P_C}{P_R} \right)^{\frac{1}{2}}}{\frac{D_C}{\sqrt{N}}}. \tag{3.1}$$

Here, L is chamber length, α is a conversion factor for chamber cooling, U_R is the propellant velocity ratio, P_R is a reference pressure, D_C is the chamber diameter, and N is the number of elements. They derived an empirical expression for c^* efficiency using this parameter and two empirical constants, A and B, shown in Equation 3.2.

$$\eta_{C^*} = 1 - A \exp\left(-B\overline{L}_C\right). \tag{3.2}$$

Based on the value of $\overline{L}_C$, they used two different sets of constants for $\overline{L}_C < 12.5$ and $\overline{L}_C > 12.5$. Correlating this data to the present study, all $\overline{L}_C$ values here were less than 12.5. The η_{c^*} data for the three values of oxygen post recess from this study versus $\overline{L}_C$ are plotted in Figure 3.6 with the reference correlation lines, also. The high correlation line uses the constants for $\overline{L}_C > 12.5$ extrapolated to values lower than 12.5, while the low correlation line uses the constants derived for $\overline{L}_C < 12.5$. The two references examined a LOX post recess of approximately one diameter. As shown in the

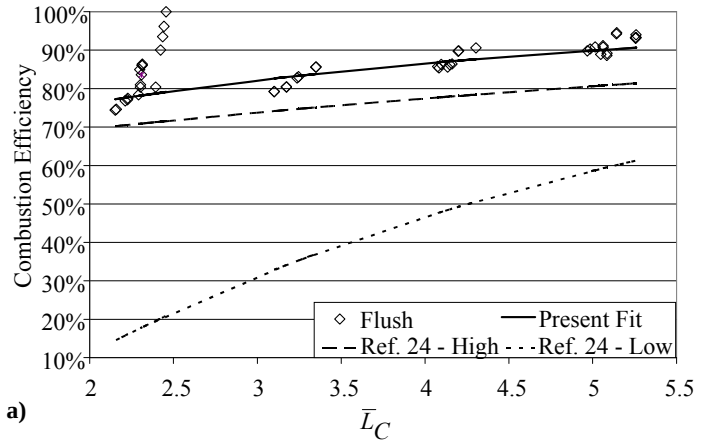

a)

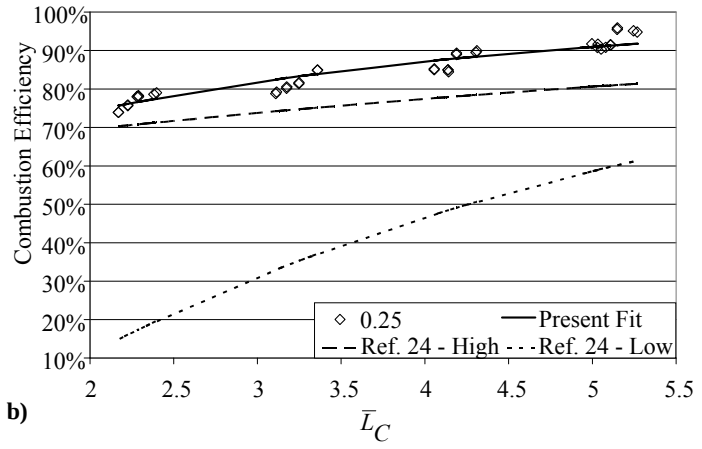

b)

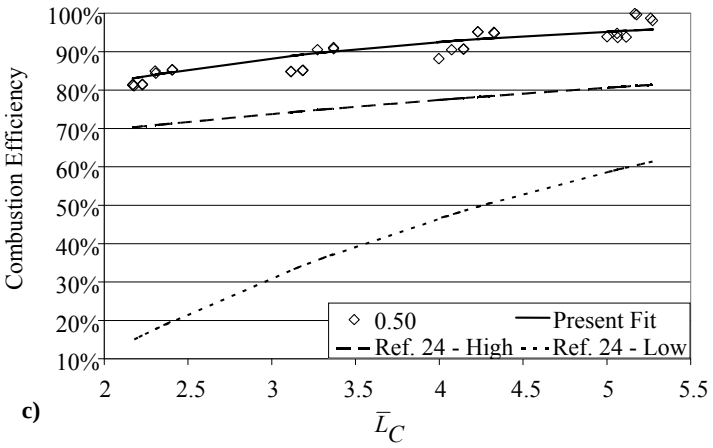

c)

Figure 3.6 Combustion efficiency data plotted against $\bar{L}_C$.
[a) Data and correlation for flush post; b) 0.25 inch recess; c) 0.50 inch recess]

Figure 3.2, the combustion efficiency increases with larger oxygen post recess, which is also evident in Figure 3.6. Table 3.2 displays the correlations used in References 37 and 38 and used presently for c^* efficiency. The terms used here were the best-fit curve to represent the current data.

Table 3.2 Correlations used in Figure 3.6.
[Tamura, et al. correlation is the same as Ref. 37-High line, which corresponds to the higher efficiency values. The Yatsuyanagi, et al. correlation relates to the Ref. 37-Low line, corresponding to lower efficiency values calculated using this correlation]

Correlation	$\eta_{c^*} =$
Tamura, et al.[38] - $\bar{L}_C > 12.5$	$1 - 0.412\exp\left(-0.151\bar{L}_C\right)$
Yatsuyanagi, et al.[37] - $\bar{L}_C < 12.5$	$1 - 1.48\exp\left(-0.255\bar{L}_C\right)$
Fig. 3.7a - No Recess	$1 - 0.42\exp\left(-0.285\bar{L}_C\right)$
Fig. 3.7b - 0.25" Recess	$1 - 0.52\exp\left(-0.35\bar{L}_C\right)$
Fig. 3.7c - 0.50" Recess	$1 - 0.45\exp\left(-0.45\bar{L}_C\right)$

Another source for comparison comes in Reference 32. The shear coaxial injector that was examined used liquid oxygen and gaseous methane as main propellants. The L^* value there was 405 inches, longer than presently studied, and the injector achieved a c^* efficiency of 85%. According to the present trends, it should have been much higher. But, liquid effects such as vaporization and atomization can tend to slow the primary reactions, leading to the need for longer combusting times and distances, and lower efficiencies. The shear coaxial injector data collected in this study served not only as

historical comparison, but also as a baseline comparison for the other three injector types in this testing system.

3.2 Swirl Coaxial Injector

The swirl coaxial injector, or swirl nut, successfully executed 22, 4-second tests. Mass flow rate calculations for the fuel verified a 0.093 inch venturi to be installed. This was not the case for the oxygen side, so no venturi was installed and flow was choked and controlled at the injector oxygen inlet. A sample firing photograph is shown is Figure 3.7 and results are presented in Figure 3.8. Results with uncertainty bars are shown in Appendix H. The legend for the results shows diamond for 2.5 mixture ratio, triangle for 3.0. No other distinctions, such as recess or chamber pressure, were made for the swirl nut as discussed earlier. First tests were performed at the 279 inch L* setting. The results were comparable with the initial shear coaxial element tests. L^* settings were then decreased according to the test matrix. The exhaust plume of the swirl nut, Figure 3.7, was more defined than the plume for the shear coaxial element, Figure 3.1. The Mach diamonds were more pronounced and the plume held a more constant shape and length during firing.

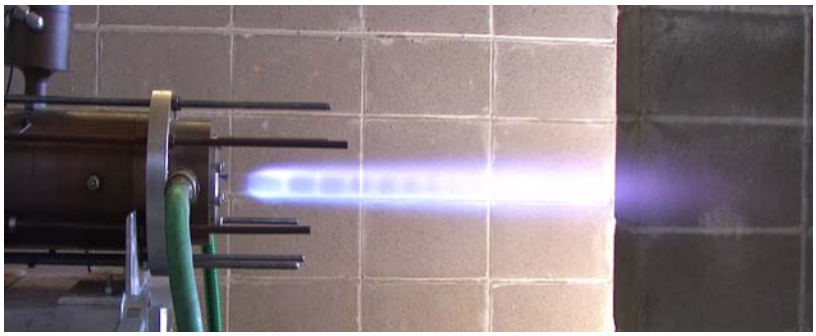

Figure 3.7 Swirl coaxial injector test firing

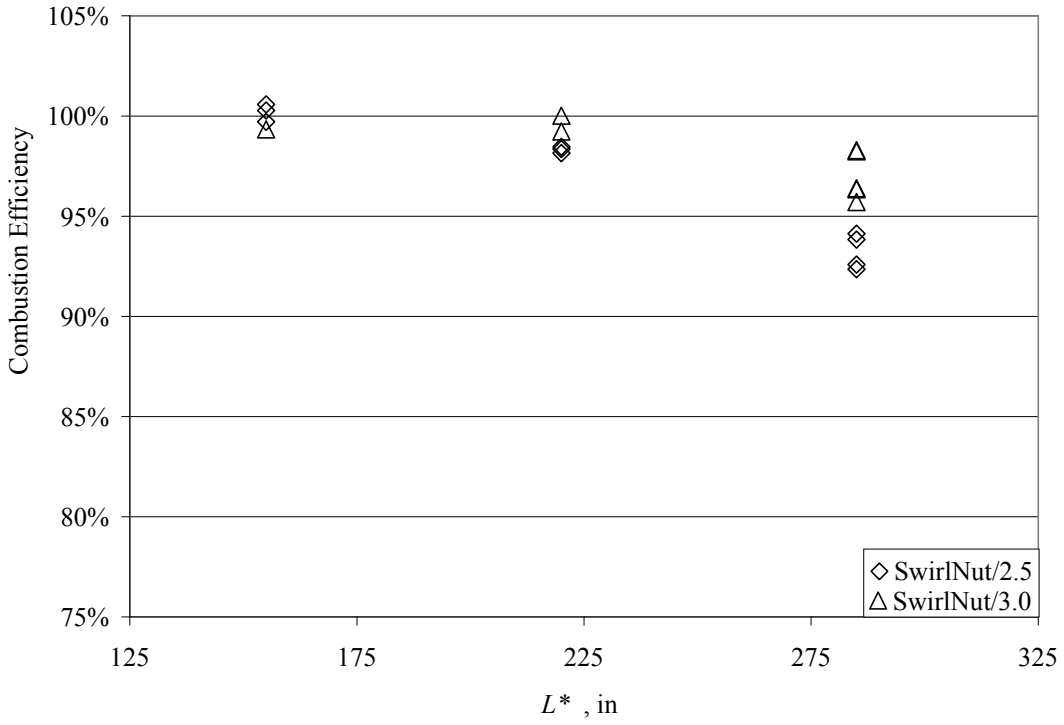

Figure 3.8 Swirl coaxial injector results. Uncertainty bars shown in Appendix H

The performance results show that combustion efficiency was highest at the shortest L^* and then decreased with increasing L^*. Because of this trend, no tests were operated at the 360 inch L^* configuration. This is a stark difference of trend compared to the shear coaxial element, Figure 3.2, where efficiency increased with L^*. The reason for this discrepancy is quite intrinsic. The mixing mechanism for a shear coaxial injector is through a turbulent mixing layer between the two propellant streams, as discussed earlier and modeled in Figure 3.9 with liquid oxygen and gaseous methane.[43] The swirl coaxial injector mixes differently. The swirling action causes the propellant to exit the injector at a "spray" angle (gaseous propellants are not typically considered to have spray angles),

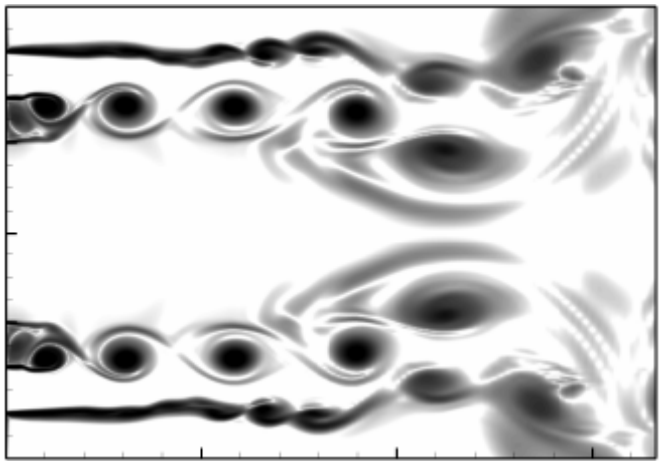

Figure 3.9 Shear coaxial mixing model of LOX and gaseous methane[43]

which divides the injection velocity into two components, axial and circumferential. The axial component moves the propellant downstream while the circumferential component forces an impingement onto the other propellant. Swirling also assists propellant breakup and atomization for liquid propellants and more efficient mixing for liquids and gases. This mixing is shown schematically in Figure 3.10. The better mixing for this element provides for efficient combustion at shorter downstream distances. The decreasing performance trend versus L^* was later attributed to heat transfer to the chamber walls.

Unlike the shear coaxial tests, maximum outside chamber temperatures were recorded for three tests. Each recording was taken from the first full test in a series, i.e., the first test of the day for the three L^* settings. These showed an increase in temperature of 25°F, 20°F, and 14°F at 279 inches, 214 inches, and 149 inches, respectively. Using Equation 2.8, relative chamber temperatures were calculated based on a theoretical chamber temperature of 5738°F, given by ProPEP. The relative temperatures were 3308°F, 3828°F, and 4348°F, for the respective L^* values. These show that a

considerable amount of heat was lost at the longer L^* for the more efficiently mixing and performing swirl nut.

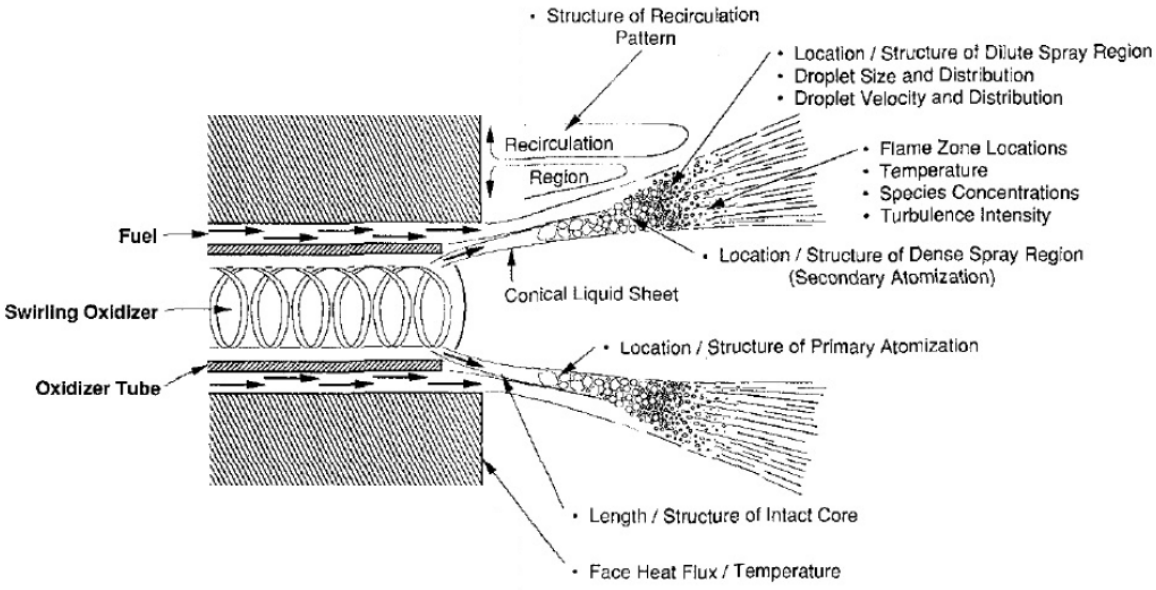

Figure 3.10 Swirl injector mixing schematic[7]

Pressure drop calculations were another factor attributed to swirl nut performance. The swirl nut design was based on a desired pressure drop (Appendix F), so statistics were desired. Table 3.3 lists the pressure drop data. In light of the concerns described in the previous section, the swirl coaxial element behaved above the desired standard of 20% pressure drop across the injector. Standing out in this data set, though, is the extremely high values for the oxygen side. As stated earlier, no rate-controlling venturi was installed there, so the oxygen flow was choked and controlled at the injector oxygen inlets because they were the smallest orifices in the line. This did not affect the combustion efficiency of the injector, though, as a 0.060 inch venturi was installed during

Table 3.3 Swirl nut pressure drops per L^* setting

L^*	ΔP_{ox}	Std Dev	ΔP_f	Std Dev
279	390.2%	10.1%	31.7%	8.8%
214	371.1%	11.3%	29.7%	5.7%
149	369.2%	15.8%	25.3%	5.0%

tests using the acrylic chamber section and no noticeable deviation was seen in performance results. The only exception to this was the increased efficiency due to burning of acrylic and rubber, as mentioned earlier. These higher performance results were thus excluded from final analysis, similar to the shear coaxial injector. Figure 3.11 shows two snapshots from the high-definition camera of the swirl nut performance. Figure 3.11a shows the spray angle from the injector, roughly 90 degrees, taken when the acrylic section cracked. This accident decreased the combustion enough such that the bright flame at 250 psi diminished and a lower pressure flame was seen, at about 75 psi when the photograph was retrieved. The other picture, Figure 3.11b, shows the swirling action from the injector during the final moments of combustion, when the nitrogen purge gas was flown. The yellow flame is indicative of a very fuel-rich environment. This was because the oxygen feed line was shut off first in order to prevent burning of chamber components, as controlled by the PLC timings in Appendix D.

In addition to direct comparison with the shear coaxial injector, the swirl nut was also compared to historic research data. There was no source for comparison of performance versus chamber length for swirl coaxial elements like the shear element. So, comparison of performance results with specified L^* values were evaluated. In Reference 8, two swirl injectors were studied and compared with a shear coaxial injector. At an L^* of 414 inches, they calculated c^* efficiencies of 94.8% and 90.9% for the two

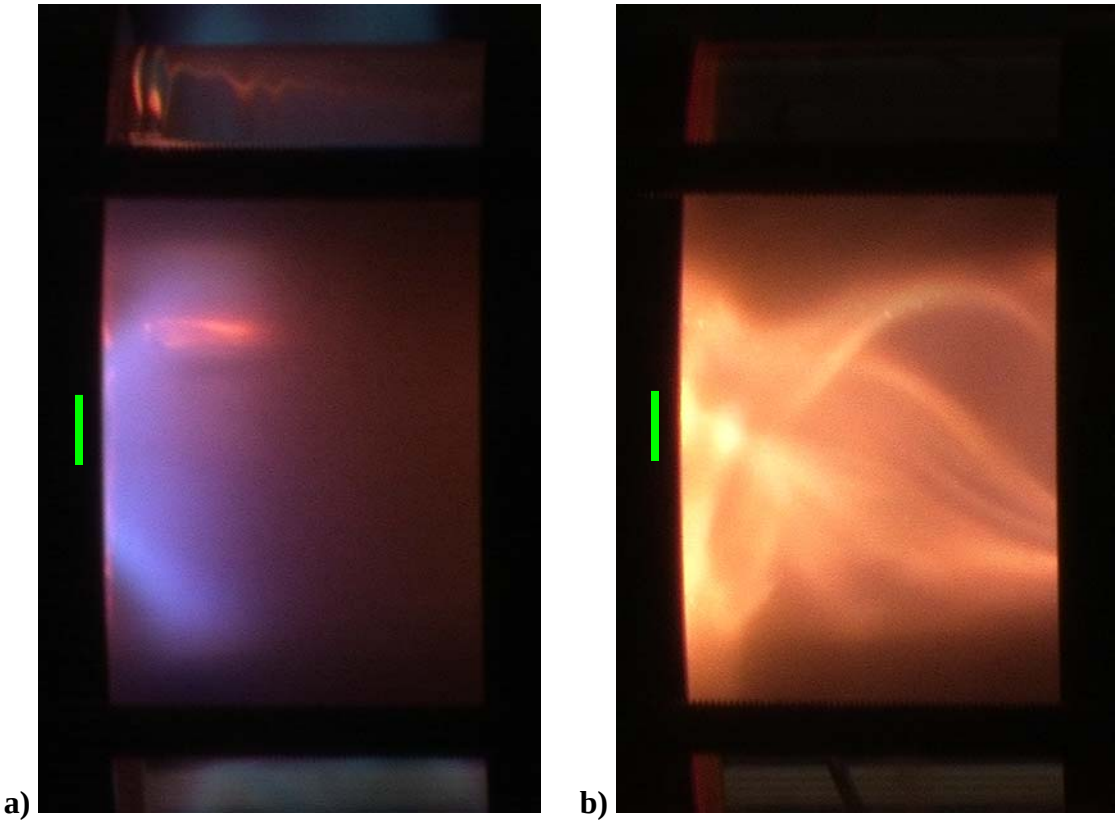

Figure 3.11 Close-up photographs of swirl coaxial injector.
[The green line marks the injector face. a) Spray angle of flame; b) Swirling action during purge. Pictures taken using acrylic chamber section]

respective elements. For the characteristic chamber length, the efficiencies seem high according to the present trend, even while the reference used liquid oxygen and gaseous methane main propellants. Reference 8 reported that these are averaged efficiency values, but did not report a standard deviation or uncertainty with their calculations. It was also not mentioned whether any correction for heat loss, momentum pressure loss, or correction for discharge coefficient were included in their final analysis. In a similar study, Reference 32 reported combustion efficiency values of 95% and 91% for an L^* of 405 inches. These results were nearly identical to Reference 8. But, there was also no

report of uncertainties or accounted losses in Ref. 32. Another source, Ref. 43, used a much shorter L* of 28 inches and reported c* efficiencies between 96 – 100%. The propellants were liquid oxygen and liquid hydrogen, which has much faster combustion than methane-oxygen, about 19 elementary reactions versus 277, respectively.[1] This may have been a factor for higher efficiency values.

3.3 Cross Flow Injectors

The cross flow injector testing was performed on two elements with similar designs. The stainless steel screw swirl injector was a first generation design, described in Reference 25. The copper screw swirl injector was an enhanced version to provide better mixing. Testing began with the stainless steel injector after the swirl nut testing was completed. Venturies used were the same as the shear coaxial injector. The durability of the material under the high temperature conditions was questionable, so 2 second tests were ran, starting at the 279 inch L^* setting. The heat conductivity of stainless steel is much less than copper, 8.1 $\frac{BTU \cdot ft}{h \cdot ft^2 \cdot °F}$ versus 226 $\frac{BTU \cdot ft}{h \cdot ft^2 \cdot °F}$, respectively. Thus, the stainless steel acted like an insulator. The first operational test showed very similar results as the swirl nut, with one exception. Instead of the characteristic blue plume, a bright orange plume was seen and ended with a small shower of sparks exiting the nozzle. Data was quickly analyzed and the injector face was examined by looking down the chamber. Performance data was comparable to the swirl nut at the same configuration and the face seemed only slightly discolored. A duplicate trial was run a few minutes later, which had the same color plume and even more sparks at the end. Testing was ended and the chamber was disassembled to reveal a damaged injector that was disqualified for any further testing. A photograph of the stainless steel

injector after testing is shown in Figure 3.12. Combustion efficiency results were 94.6% for the first run and 92.1% for the second run, but due to damage and the large difference in efficiency between the two trials, they were not included in final analysis. But, lessons were learned and used in the next series of testing.

Figure 3.12 Stainless steel injector damage after firing two tests

Copper cross flow injector testing followed with much more caution as detailed earlier. The 0.093 venturi was needed for the fuel and a 0.060 venturi for the oxygen. The venturi for the latter was not available, so an orifice of the same size was installed. Because orifices have much lower flow recovery than venturies, about 50% versus 80%, respectively, the pressure drop required was also too high to conduct high chamber pressure tests, like the swirl nut. For this injector, checkout consisted of lower pressure

hot-fire tests with shorter run times. Set-point chamber pressures started with 150 psia, increasing by 50 psi after successful firings of one second. Visual inspection of the injector after each run supported a following one.

Ultimately, 14 successful 1-second firings were evaluated, 12 at a mixture ratio of 2.5 and 2 at 3.0. Results from these tests are shown with the swirl nut results in Figure 3.13. Inspection of the fire face was conducted after each firing to ensure durability. No major defect was found other than slight erosion of the screw tips, seen in Figure 3.14. The same

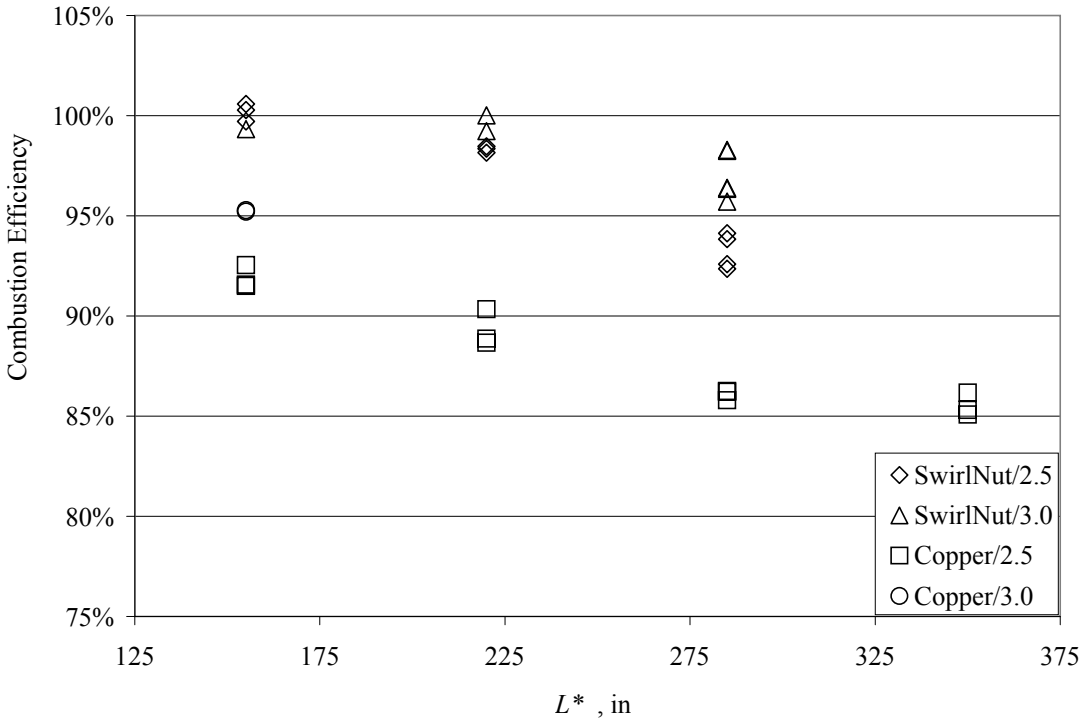

Figure 3.13 Results of copper screw swirl injector compared with swirl nut.
[Uncertainty bars shown in Appendix H]

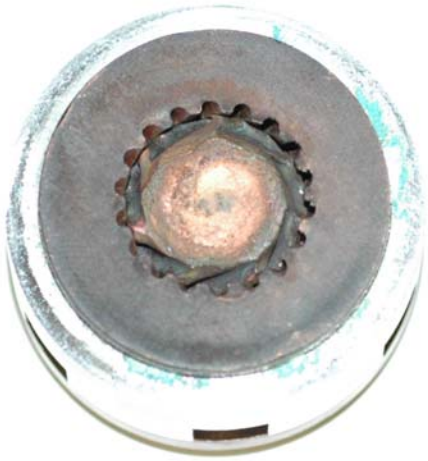

Figure 3.14 Fire face of copper cross flow injector after testing

trend of performance with L^* is seen with both swirl type injectors; that is, combustion efficiency decreased with increasing L^*. Tests were conducted at the longest L^* setting, 344 inches, in an attempt to capture more of the trend. While there was a small decrease in performance from the 279 inch setting, it was not as much of a drop as between other settings. This means that the added length of chamber did not increase the heat transfer very much. Since the copper cross flow and swirl nut trends are similar, mixing mechanisms must also be similar. But, while they may be similar, efficiency values were still lower than the swirl nut. The 3.0 *O/F* trials were last to be tested when testing was concluded due to the schedule. The two points for these tests can be used for comparison at L^* of 149 inches, but no trend can be made with the 2.5 setting. The pressure drop info is listed in Table 3.4. Pressure drop for each propellant line shows an increase with L^*, similar to the swirl nut but contradictory to the shear coaxial injector, and with a clear

distinction between the 214 inch and 279 inch setting. The shorter two configurations have lower pressure drops than the longer two, which are nearly the same. This distinction follows the combustion efficiency data, where performance behaved in the same manner. This suggests that this difference with L^* marked a definitive place where combustion was complete and the extra chamber length was unnecessary and inefficient.

Table 3.4 Copper cross flow pressure drops per L^*

L^*	ΔP_{ox}	Std Dev	ΔP_f	Std Dev
344	97.8%	2.0%	79.8%	1.9%
279	97.3%	0.3%	80.9%	0.5%
214	91.3%	1.7%	75.7%	1.8%
149	90.3%	1.4%	75.9%	1.6%

Several tests were conducted with the acrylic section. Flame propagation was very smooth and uniform, as shown in Figure 3.15. This is in contrast with the flames from the shear coaxial element and swirl nut, Figures 3.5 and 3.9, respectively. The face of the copper injector had multiple holes where the propellant exited rather than one orifice for each stream, like the two coaxial elements. The swirling action of this element was not able to be captured, though, like the swirl nut during purge. The flame for the copper injector quickly extinguished when propellants were shut off and purge was initiated. This mixing mechanism may not have been as efficient as the swirl nut, leading to lower performance values.

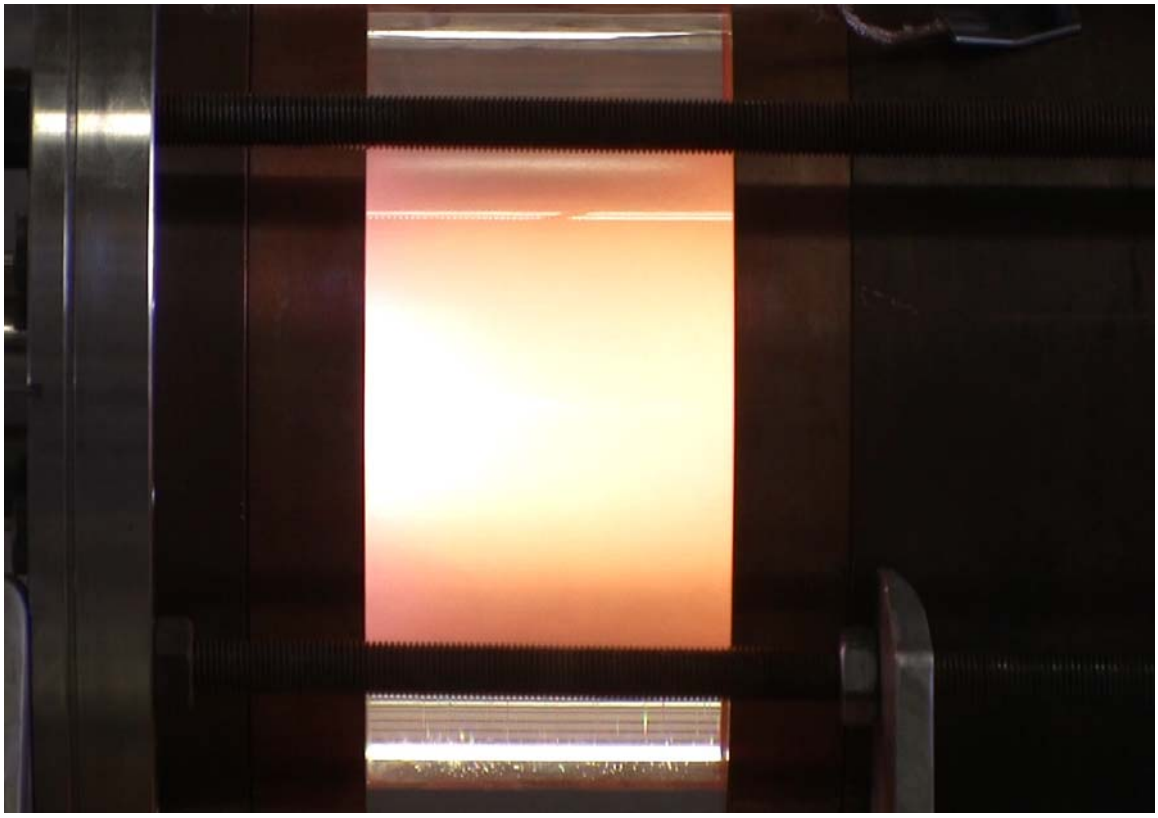

Figure 3.15 Copper cross flow injector flame using acrylic section

Comparison of pressure traces also explains performance differences. Figure 3.16 shows pressure traces from the three successful injectors at the same test condition and configuration, L^* of 279 inches, 2.5 *O/F*, and low chamber pressure. The shear coaxial and swirl coaxial elements behaved in a nominal manner, rising and reaching steady state quickly, while the copper screw swirl element lags to almost reach steady state until the test is shut down. This lag could have been a consequence of the pressure drop and flow structure of the screw element. Of course, there is less performance of this injector over the entire test time compared with the other two over an equivalent time scale. So, rather than using the middle 500 data points for efficiency calculations like the coaxial injectors,

the final 50 data points for highest pressure were used. This area represented the top 95% of the data, so steady-assumptions were made. The pressure during this time interval was very close to the steady-state pressure of the swirl nut, so efficiency could have been similar if longer testing could have been done. Nevertheless, this could have skewed the results slightly.

Temperature measurement was not recorded for these tests, so no quantitative flame comparisons could be made with the swirl nut. Also, there were no rocket engine performance data available for direct comparison with this injector. Since the same general trend with L^* was seen, similar data comparisons can be made with other swirl elements.

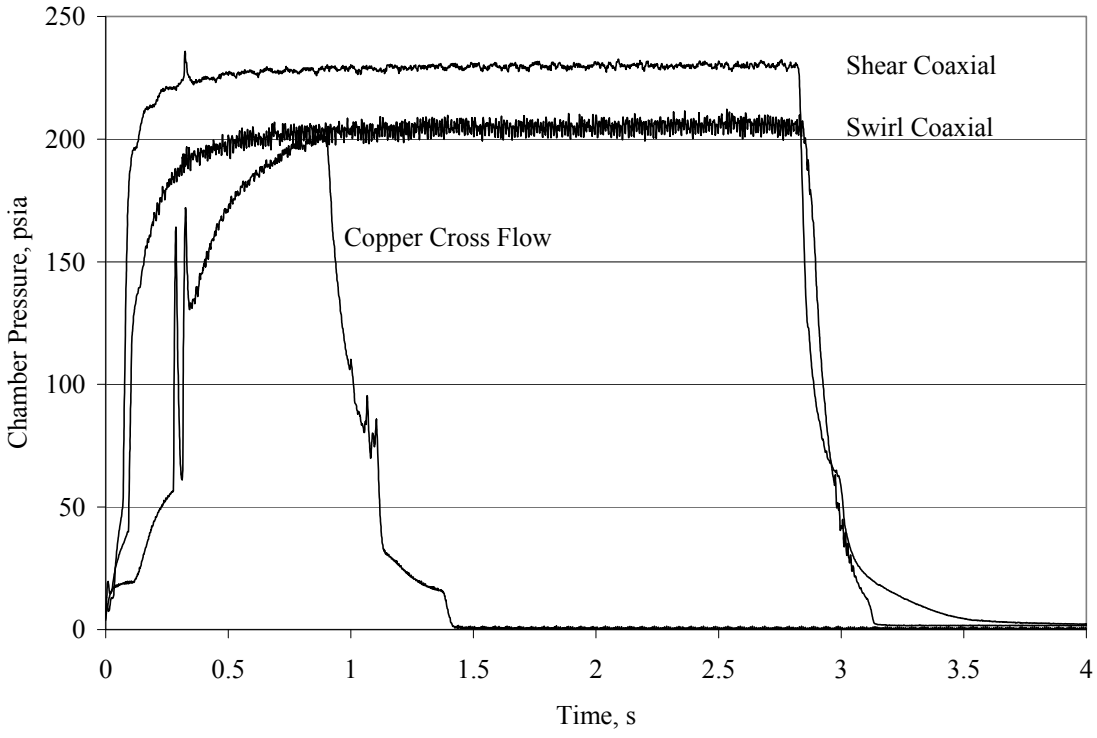

Figure 3.16 Pressure traces of three injectors during acrylic section tests.
[Characteristic chamber length was 279 inches]

3.4 Additional Observations

Several performance parameters affecting efficiency calculations were observed, but not included in the final analyses for the injectors. Several sources cite that certain engine consideration affected their final results. These include, but are not limited to, heat loss, momentum pressure loss, and the throat discharge coefficient. Already mentioned in the previous sections are considerations of heat loss, which did ultimately affect performance results. Momentum pressure loss is part of total pressure loss in the system. This was accounted for with the injector pressure drop calculations. But, overall loss was negligible due to such short distances between critical components (venturies, injectors, and injection plane) and small sizes of the injectors. The discharge coefficient of the engine nozzle throat is a function of orifice geometry and is generally taken to be 0.99 in most experiments. This was close enough to 1.0 to be excluded from final calculations.

Additional considerations taken were with respect to thermal changes. In relation to the nozzle throat, a throat radius influence factor[44] was determined. Using the largest measured temperature change of the chamber walls, this factor was calculated from Equation 3.3.

$$\Delta A_t = \frac{\pi}{4}\left(2 + \alpha_{Cu}\Delta T\right)\left(\alpha_{Cu}\Delta T\right)D_t^2 . \tag{3.3}$$

Here ΔA_t is the change in throat area, α_{Cu} is the thermal expansion coefficient of copper, and D_t is the throat diameter. The influence factor, f_{TR} was then calculated by

$$f_{TR} = 1 + \frac{\Delta A_t}{A_t}, \tag{3.4}$$

which was 1.00049. Even assuming a supposed temperature increase of 400°F, the influence factor would only be 1.0075. So, this factor was excluded from final analysis for two reasons. First, the measured temperature change was of the chamber wall and not the nozzle. Heat flux is much higher at the nozzle throat than anywhere else on the chamber, so temperature change may have been higher. Second, the value is so small it was negligible. These and other correction factors could have been included in the final data analysis, but the values were within uncertainty and where ultimately excluded.

Another testing observation was the number of acrylic sections installed on the chamber. Four acrylic sections were ultimately used, two of which broke during firing. The first section lasted through four swirl nut firings. The 4 second burn time caused too much erosion to be deemed safe for operation. Another section was installed and all acrylic tests were limited to 2 seconds. The second section broke on the last swirl nut firing. It cracked along the wall axially, as shown in Figure 3.17. The piece used for the shear coaxial firings lasted for all of the tests, with different erosion levels for different chamber configurations as shown in Figure 3.18. The fourth section used during the copper injector tests cracked in the same manner as previously after four tests. It was thought that too much axial stress was applied from the compression rods, but safety calculations negated that. Finally, damage was thought to have occurred due to pressure shock at initial injection. The repetitive impulse of pressure at the onset of combustion was a likely cause of damage. Another factor that could have led to damage was high heat flux from the swirl tests. The propellants burned at an angle close to the acrylic wall, whereas the shear coaxial injector burned propellants primarily axially. The flame was centered in

Figure 3.17 Broken acrylic chamber section

Figure 3.18 Acrylic section from shear coaxial injector studies

the chamber so the excess methane (fuel-rich mixture ratio) could fill the remaining volume, which prohibited high heat fluxes and kept the acrylic section intact.

A characteristic of swirl injectors commonly used is the swirl number. It is a function of spray angle, or spray velocity components in the axial and tangential directions, and injector geometry. The swirl number, S, is calculated by

$$S = \frac{\int_{R_O}^{R_G} uwr^2 dr}{R_G \int_{R_O}^{R_G} u^2 r dr}, \tag{3.5}$$

where u and w are axial and tangential velocity, respectively, and R_G and R_O are outer and inner radii, respectively. Based on the swirl nut calculations, which were also used for the cross flow injectors, swirl numbers were calculated and summarized in Table 3.5. The values for the swirl nut and stainless steel cross flow injectors are the same because the spray half angle for the swirl nut is the same as the screw angles of the stainless element, 45 degrees. The swirl number for the oxygen in the copper element is so high because of the wide angle from the screw nut, Table 2.3. This difference in swirl numbers may have been a cause for variation in performance. But, comparison of this parameter could not be made between the two cross flow injectors because of damage to the stainless steel element. The swirl number parameter can be used for comparison with other swirl injector designs.

Table 3.5 Swirl numbers for each injector and propellant

Injector	S_f	S_{ox}
Swirl Nut	1.504	0.892
SS Cross Flow	1.504	0.892
Copper Cross Flow	0.867	2.373

Measurement uncertainties were another factor of testing. The pressure drop information in the previous chapter lists averages along with standard deviations. Standard deviations represent just part of the total uncertainty, which was calculated for all tests, and shown for 344/Flush/2.5/HighP and 149/Flush/2.5/LowP, in Appendix H. Monte Carlo simulations of 500 trials were run to calculate combustion efficiency uncertainty. Using the data reduction equation of Equation 2.5 factored to depend only on the measured variables of chamber pressure, propellant stagnation pressures and temperatures, throat diameter, and venturi diameters, these simulations most completely described the mathematics of the efficiency calculation, albeit assuming normal distributions of the variables. In general, for low pressure and high pressure tests, the uncertainty was approximately 2.5% and 1.5%, respectively. Injector performance results, Figures 3.2 and 3.13, are shown in Appendix H with uncertainty bars. The trends of combustion efficiency with L^* are still valid with the uncertainties included.

Uncertainty was also calculated for L^*. Using Equation 2.1 as the data reduction equation, relative uncertainties for L^* settings of 149, 214, 279, and 344 inches were about 1.3%, 1.2%, 1.2%, and 1.3%, respectively, which equate to 1.9, 2.6, 3.4, and 4.3 inches, respectively. These were not included in the figures presented in Appendix H for clarity and that the uncertainty bars were smaller than the data points.

Another source for comparison, Reference 36, showed no discernable difference in combustion efficiency between chamber lengths of 9 and 13 inches using an impinging injector with LOX/Methane. This was because the mixing zone for this injector type is much shorter than shearing types. Based on the flame images for the swirl injectors,

flame propagation for an impinging injector should be equivalent, if not shorter. So, performance differences should not have been observed based on the present trends.

CHAPTER 4

CONCLUSIONS AND RECOMMENDATIONS

Test data and characterization of the four injectors examined were compared with each other and with historical designs. Information gathered from each injector type can be used for future comparison and aid for new injector concepts. Data can also be used to correlate with other propellant combinations for similar injector designs. This study can also aid in the design of combustion chambers and other combustors in order to achieve the highest combustion efficiency for a given injector scheme.

4.1 Conclusions

The effects of characteristic chamber length on combustion efficiency of a small rocket engine using GOX/Methane propellants with four injectors of three types have been examined. The main contributors to influence combustion efficiency were L^* for all injector types, and chamber pressure and oxygen post recess for the shear injector. Little to no effects of mixture ratio and velocity ratio on c^* efficiency were found for the ranges tested in this study.

The two designed set points for chamber pressure were 250 and 500 psia. This factor had a significant effect on combustion efficiency of the shear coaxial element. This parameter was unable to be examined for the other three injectors due to injector

geometry. For every chamber and injection configuration, the higher chamber pressure tests obtained higher efficiencies than the lower chamber pressure tests. On average, the higher pressure provided about 4% higher efficiency values.

The oxygen post recess was another major contributor to combustion efficiency for the shear coaxial injector. In general, recess allowed earlier and more mixing, thus higher efficiency; additional recess positively affected this trend. There was only a slight increase in combustor performance when the oxygen post was recessed one diameter, less than one percent increase. When recessed two diameters (0.50 inches) efficiency values increased on average 4.5 percent for all L^* configurations. While these factors were of major influence, changing L^* had the greatest effect on combustor performance.

Combustion efficiency was evaluated at four values of characteristic chamber length: 149, 214, 279, and 344 inches. The characteristic length had a direct influence on the residence mixing time, and thus mixing efficiency, of the propellants; that is, for a shorter L^* value, there is less time allowed for propellant mixing. It has been shown that for a shear coaxial injector, the limiting factor is this mixing efficiency and a larger L^* is required to achieve higher combustion efficiencies. For a swirl coaxial injector, mixing was very efficient, requiring a lower L^* to obtain higher efficiency. A higher value of L^* actually resulted in decreased swirl injector efficiency, mainly due to heat loss through the copper chamber walls. This was also the case for the copper cross flow element. In general, it was found that increasing L^* increased combustion efficiency for a shear coaxial injector and decreased efficiency for the swirl injectors. On average, the increase of shear injector efficiency from the lowest to highest L^* was approximately 12%, per

injection scheme; decrease of swirl coaxial injector performance was about 5%; and about 6% decrease of cross flow injector performance.

One configuration of the shear coaxial injector led to a deviation from this trend, which was the setup of the lowest L^*, flush oxygen post, 2.5 mixture ratio, and high chamber pressure. The unstable combustion observed at this configuration enhanced propellant mixing, providing higher efficiencies than the steady cases. Visual verification of this phenomenon was attempted using an acrylic chamber section but was unsuccessful.

The data gathered from the shear element was compared with historical data of small scale engine performance using propellant combinations of LOX/Hydrogen and LOX/Methane. Because gaseous oxygen was used in this study, data were not expected to exactly match with reference data. Rather, the trend of combustion efficiency with chamber length was expected to be similar. This was verified with reference correlations applied to the present data.

Measurement of the combustion chamber outside walls showed an increase of 25^oF at an L^* of 279 inches, while the 149 inch L^* chamber had an increase of only 8^oF during tests of the swirl coaxial element. This showed a large discrepancy between the theoretical flame temperature and the calculated relative temperature. The large difference suggested that combustion efficiency values should have been lower. But, the measured temperature value was very uncertain because the temperature trace for each test was not completely recorded; only a maximum value shortly after a trial was completed. Also, since most other tests did not record temperature data, this discrepancy

could not be substantiated. Despite such setbacks, performance testing and injector characterization was successful.

4.2 Recommendations for Future Tests

Several operational recommendations can be advised for this kind of injector testing. More injectors of the same types, but different sizes and parameters should be examined. Additionally, injectors that are currently used in production engines should be examined as a benchmark for this methodology. Also, different injector types should be investigated, such as impinging injectors. The engine could also be adjusted. Since L^* is dependent on chamber volume and nozzle throat area, nozzles of different areas could be installed; also, changing chamber volume by chamber diameter rather than length should be investigated and compared with current results. Effects of chamber cooling could also be examined. A water-cooled chamber or film-cooling techniques could be investigated. Additional characterization methods should be implemented, such as chemiluminescence, in order to obtain more quantitative results for flame behavior. The unstable and rough tests should be run again with a microphone located near the nozzle in an attempt to capture the frequency of instability if it should be there, similar to what was done in Reference 18.

More direct to the current system, different propellants should be tested with the same hardware. Effects of the propellants under the same operating conditions would provide great insight to the combustion and performance inside the rocket engine. Also, preburner conditions might be of interest for injector design comparison. Specific to the cross flow elements, injector cooling might be examined. Porous or sintered materials could be used so fuel could cool the side exposed to the fire face. Application of these

recommendations could ultimately provide more efficient injector and chamber designs for future rocket engines.

APPENDICES

APPENDIX A

Test Procedures

Note: These operational procedures are part of a safety manual for conducting engine tests developed by the author, faculty, and staff of the Propulsion Research Center.

Test Stand Preparation

- Open all gates
- Attach pressurization air to actuated fire valve air manifold on the back of the test stand (plastic tubing)
- Attach the pressurization air to the compressor in the instrumentation room and make sure that the compressor is on auto compress
- Ensure air compressor tank pressure is at least 80 psi
- Attach the water line from the instrumentation room to the quick disconnect fitting on the nozzle.
- Attach water drainage line
- Put up all blockades around the test facility

Igniter Setup

- Attach blue igniter ground to actuator grounding post
- Attach oxygen line to the igniter
- Attach hydrogen line to the igniter
- Clamp grounding clamp to the copper plate behind the thrust stand
- Set the secondary oxygen needle valve to the correct setting (Default: 5)
- Set the secondary hydrogen needle valve to the correct setting (Default: 5)

Instrumentation

- Check the *Sensor Locations Sheet* for proper set-up channels with correct pressure sensors and/or thermocouples
- Set up video camera to view the nozzle and plume. Hook up RCA cables, BNC cable, and power cord. (ensure camera is in focus)
- Turn on LabView and open the *LabVIEW Operating Program*
- Press RUN and ensure program is running properly
- Type in the appropriate *LabVIEW Data Record* filename
- Press RECORD and press STOP after 5 seconds. This will record a zeros file

Ensure LabVIEW recorded properly

Control Room Settings

- Ensure PLC times are correct in *CXOne PLC Program*, referencing the *PLC Timing Sheet*
- Upload PLC timing values to PLC within *CXOne PLC Program* under the *Memory* tab
- Make sure test facility area is clear
- Insert key and Toggle all valves
- Insert enable plug
- Press Reset on the control board
- Press FIRE on the control board
- Ensure the actuators are functioning properly

Water Leak Check (Only needs to be performed when installed at beginning of testing and when equipment is changed)

Cooling Lines

- Place the drainage line of the water hose in the drain
- Open water main line in the instrumentation room
- Remove Nozzle Plug or tape over nozzle
- Ensure that there is no leakage from the H2O system

Propellant Line Fill

- With all Red Team members in the control room, use the control board to switch on the **ox main, ox primary dome, ox secondary dome, fuel main, fuel primary dome, fuel secondary dome**
- Remove the key from the control board
- Give test engineer control key
- Open the nitrogen ball valves on the nitrogen manifold
- Crack open tanks to slowly bleed in pressure
- Completely open nitrogen tanks
- Ensure that there is sufficient pressure in the manifold
- Adjust the pressure settings to the appropriate pressures, according to the Pressure Board Settings Table below and Table 1

- Commence Purge Check Sequence, next
- Replace key and turn on board
- Switch on fuel primary purge
- Confirm injector purge flow from video
- Switch off fuel primary purge, switch on fuel secondary purge
- Confirm igniter purge flow from video
- Switch off fuel secondary purge, switch on ox primary purge
- Confirm injector purge flow from video
- Switch off ox primary purge, switch on ox secondary purge
- Confirm igniter purge flow from video
- Switch off ox secondary purge

- Close vent to igniter fuel manifold
- Open the ball valve to the igniter fuel manifold
- Crack open the igniter fuel tank to slowly bleed in pressure
- Completely open igniter fuel tank
- Ensure that there is sufficient pressure in the manifold (at least 3 times operating pressure)
- Close vent to Oxygen igniter manifold
- Open the Oxygen Igniter ball valve on the Oxygen Igniter manifold
- Crack open the Oxygen igniter tank to slowly bleed in pressure
- Completely open Oxygen igniter tank
- Ensure that there is sufficient pressure in the manifold (at least 3 times operating pressure)
- Make sure that the pressure settings are correct on the pressure regulator board and record

Firing Sequence

1st Firing – Igniter test, no spark

- Run *LabVIEW Operating Program*
- Make sure test facility area is clear
- Check to make sure all Red Team members are in the control room and that the **ox main, ox primary dome, ox secondary dome, fuel main, fuel primary dome, fuel secondary dome** are switched on
- Ensure that all test stand pressures are correct
- Hit record on the DVD recorder
- Announce the Test Number and what test it is
- Press Reset

Insert enable plug

- Press FIRE on the control board
- After sequence is complete press Reset and remove the Enable Key and Switch Key
- Stop the LabVIEW program
- Ensure LabVIEW recorded to the appropriate file name
- Record igniter and chamber pressures Chamber: _____ Igniter: _____

2nd Firing – Igniter test with spark

- Give test engineer control key
- Attach red spark plug connection to the spark plug tip on the igniter
- Make sure test facility area is clear
- Ensure that all test stand pressures are correct
- Hit record on the DVD recorder
- Announce the Test Number and what test it is
- Press Reset
- Insert enable plug
- Press FIRE on the control board
- After sequence is complete press Reset and remove the Enable Key and Switch Key
- Stop the LabVIEW program
- Ensure LabVIEW recorded to the appropriate file name
- Record igniter and chamber pressures and ensure higher values

Chamber: _____ Igniter: _____

3rd Firing – Main propellants included

- Give test engineer control key
- Close vent to Fuel Main manifold
- Open the Fuel Main ball valves on Fuel Main manifold
- Crack open the Fuel Main tanks to slowly bleed in pressure
- Completely open tanks
- Ensure that there is sufficient pressure in the manifold (at least 2 times operating pressure)
- Close vent to Oxygen Main manifold
- Open the Oxygen Main ball valves on Oxygen Main manifold

- Crack open the Oxygen Main tanks to slowly bleed in pressure
- Completely open tanks
- Ensure that there is sufficient pressure in the manifold (at least 2 times operating pressure)
- Make sure test facility area is clear
- Ensure that all test stand pressures are correct
- If dome pressures are not holding constant, perform following 4 procedures; otherwise, skip ahead
    - If needed, open and flow Primary Oxidizer to bring Oxygen to Ox Fire Valve
    - If needed, Primary Fuel Fire Valves to bring Fuel to Fuel Fire Valve
    - If needed, purge the Primary Oxidizer
    - If needed, purge the Primary Fuel

  ***********Repeat tests can begin from here*************
- Hit record on the DVD recorder
- Announce the Test Number and what test it is
- Press Reset
- Insert enable plug
- Press FIRE on the control board
- After sequence is complete/purged press Reset and remove the Enable Key and Switch Key
- Stop the LabVIEW program
- Ensure LabVIEW recorded to the appropriate file name

Shut-Down Sequence

- Close Main Fuel tanks
- Vent Main Fuel manifold
- Close Main Fuel Manifold Ball valves
- Close Main Oxygen tanks
- Vent Main Oxygen manifold
- Close Main Oxygen manifold ball valves
- Close Igniter Fuel tank
- Vent Igniter Fuel manifold
- Close Igniter Fuel manifold ball valves
- Close Igniter Oxygen tank
- Vent Igniter Oxygen manifold

- Close Igniter Oxygen manifold ball valves
- Ensure all personnel are in the control room
- Purge all lines with Nitrogen
- Close all Domes and Mains
- Turn off all switches
- Close Nitrogen tanks
- Vent Nitrogen manifold

- Close Nitrogen manifold ball valves
- Ensure all pressures are back to ambient with LabVIEW
- Turn off water
- Detach water line
- Detach actuator air line from the compressor
- Detach instrumentation and store camera in instrumentation room

Failure Analysis

FAILURE MODE	MITIGATION	SOLUTION	EFFECT
Gas leaks in supply lines	Leak check before test	Leak Check	
Power failure	Shut-down sequence when power returns	Fuel vent valve releases fuel to drainage. Close Tanks and vent	
Missed ignition	Try sequence once more or adjust PLC timing/ injector ignition operating conditions	Press BRB on the test stand control box and reset control switches. Stop LabVIEW.	Unburned propellants in test stand
Inadvertent Burning of Experiment	Ensure fuel-rich mixture. Ensure propellant flows are correct with LabVIEW.	Press BRB on the test stand control box and reset control switches. Stop LabVIEW.	Damaged components
Over Pressurization	All parts rated for higher pressures than supply pressure. Combustion pressure is also lower than rated parts.	Press BRB on the test stand control box and reset control switches. Stop LabVIEW. Check for damaged parts.	Shut-down sequence and assess failure location and possible damage. Nozzle proven to be first part to fail. Nozzle is calculated to eject towards retaining wall. Reference Appx. 3
No Cooling Water	Check water flow prior to firing.	Connect water hose. Assess any damage to nozzle.	Nozzle could erode.
Accidental ignition or start of gas flow	Key ignitions, follow ignition procedure	Press BRB on the test stand control box and reset control switches. Close all valves. Shut off K-bottles.	Combustible mixtures may be present in test stand.
Experiment will not stop	Check PLC Timing and valve operation. Purge sequence is initiated after firing.	Press BRB on the test stand control box and reset control switches. Stop LabVIEW. Turn key off. Close switches. Remove Enable plug.	Damage to parts
Combustible gas meter alarm	Leak check	Close valves, vent, and wait for alarm to stop	Combustible mixtures may be present in test stand.

APPENDIX B

Safety Considerations

Thick Wall Hoop Stress

$P_i := 1000psi$ $P_o := 14.7psi$ $r_o := 2.5in$ $r_i := 1.0625in$

$Su_{cu} := 220 \cdot 10^6 Pa$ $Sy_{cu} := 70 \cdot 10^6 Pa$

$$\sigma_c := \frac{P_i \cdot r_i^2 - P_o \cdot r_o^2}{r_o^2 - r_i^2} - \frac{r_i^2 \cdot r_o^2 \cdot (P_o - P_i)}{r_o^2 \cdot (r_o^2 - r_i^2)} \qquad \sigma_c = 2.894 \times 10^6 Pa$$

$$FS := \frac{Sy_{cu}}{\sigma_c} \qquad \boxed{FS = 24.19}$$

Nozzle Bolt Stress

$Sy_{ss} := 205MPa$ $D_{bolt} := .25in$

$$F_{bolts} := P_i \cdot \pi \cdot r_i^2 \qquad F_{bolts} = 3.547 \times 10^3 lbf$$

$$F_b := \frac{F_{bolts}}{8} \qquad F_b = 443.32lbf$$

$$\sigma_{c.b} := \frac{F_b}{D_{bolt}^2 \cdot \frac{\pi}{4}} \qquad \sigma_{c.b} = 9.031 \times 10^3 psi$$

$$FS_b := \frac{Sy_{ss}}{\sigma_{c.b}} \qquad \boxed{FS_b = 3.292}$$

Mounting Bolt Stress

$Thrust := 500lbf$

$\Sigma M_A := 0$ $\Sigma M_B := 0$

$\frac{Thrust}{2} \cdot 3in - B_y \cdot 6in := 0$ $\frac{Thrust}{2} \cdot 3in + A_y \cdot 6in := 0$

$\Sigma F_x := 0$ $\Sigma F_y := 0$

$\frac{Thrust}{2} - A_x - B_y := 0$ $A_y + B_y - W := 0$

$A_x := 125lbf$ $B_x := 125lbf$

$A_y := 125lbf$ $B_y := 125lbf$

Shear $\sigma_{sh} := \frac{A_x}{D_{bolt}^2 \cdot \frac{\pi}{4}}$ $\sigma_{sh} = 2.546 \times 10^3 psi$

Tension or Compression $\sigma_t := \frac{A_y}{D_{bolt}^2 \cdot \frac{\pi}{4}}$ $\sigma_t = 2.546 \times 10^3 psi$

Resultant $:= \sqrt{\sigma_{sh}^2 + \sigma_t^2}$ $Resultant = 3.601 \times 10^3 psi$

$FS_{mb} := \frac{Sy_{ss}}{Resultant}$ $\boxed{FS_{mb} = 8.256}$

$Su_{shear.ss} := 20305psi$

$FS_{mb.sh} := \frac{Su_{shear.ss}}{\sigma_{sh}}$ $\boxed{FS_{mb.sh} = 7.974}$

Chamber Compression Rods

$D_{eff.rods} := 3in$ $D_{rod} := .3125in$

$Force := P_i \cdot D_{eff.rods}^2 \cdot \frac{\pi}{4}$ $Force = 7.069 \times 10^3 lbf$

$Force_{rod} := \frac{Force}{8}$ $Force_{rod} = 883.573lbf$

$\sigma_{c.rod} := \frac{Force_{rod}}{D_{rod}^2 \cdot \frac{\pi}{4}}$ $\sigma_{c.rod} = 1.152 \times 10^4 psi$

$FS_{rod} := \frac{Sy_{ss}}{\sigma_{c.rod}}$ $\boxed{FS_{rod} = 2.581}$

Chamber compression rods most likely to fail first

APPENDIX C

Test Matrices

Table C.1 Shear coaxial test matrix

Test Name	L^*, in	Recess, in	P_C, psia	O/F	$\dot{m}_{ox}$, lbm/s	$\dot{m}_f$, lbm/s
149/Flush/2.5/LowP	149	0	250	2.5	0.1	0.04
149/Flush/3.0/LowP	149	0	250	3.0	0.105	0.035
149/Flush/2.5/HighP	149	0	500	2.5	0.2	0.08
149/Flush/3.0/HighP	149	0	500	3.0	0.21	0.07
149/0.25/2.5/LowP	149	0.25	250	2.5	0.1	0.04
149/0.25/3.0/LowP	149	0.25	250	3.0	0.105	0.035
149/0.25/2.5/HighP	149	0.25	500	2.5	0.2	0.08
149/0.25/3.0/HighP	149	0.25	500	3.0	0.21	0.07
149/0.50/2.5/LowP	149	0.50	250	2.5	0.1	0.04
149/0.50/3.0/LowP	149	0.50	250	3.0	0.105	0.035
149/0.50/2.5/HighP	149	0.50	500	2.5	0.2	0.08
149/0.50/3.0/HighP	149	0.50	500	3.0	0.21	0.07
214/Flush/2.5/LowP	214	0	250	2.5	0.1	0.04
214/Flush/3.0/LowP	214	0	250	3.0	0.105	0.035
214/Flush/2.5/HighP	214	0	500	2.5	0.2	0.08
214/Flush/3.0/HighP	214	0	500	3.0	0.21	0.07
214/0.25/2.5/LowP	214	0.25	250	2.5	0.1	0.04
214/0.25/3.0/LowP	214	0.25	250	3.0	0.105	0.035
214/0.25/2.5/HighP	214	0.25	500	2.5	0.2	0.08
214/0.25/3.0/HighP	214	0.25	500	3.0	0.21	0.07
214/0.50/2.5/LowP	214	0.50	250	2.5	0.1	0.04
214/0.50/3.0/LowP	214	0.50	250	3.0	0.105	0.035
214/0.50/2.5/HighP	214	0.50	500	2.5	0.2	0.08
214/0.50/3.0/HighP	214	0.50	500	3.0	0.21	0.07
279/Flush/2.5/LowP	279	0	250	2.5	0.1	0.04
279/Flush/3.0/LowP	279	0	250	3.0	0.105	0.035
279/Flush/2.5/HighP	279	0	500	2.5	0.2	0.08
279/Flush/3.0/HighP	279	0	500	3.0	0.21	0.07
279/0.25/2.5/LowP	279	0.25	250	2.5	0.1	0.04
279/0.25/3.0/LowP	279	0.25	250	3.0	0.105	0.035
279/0.25/2.5/HighP	279	0.25	500	2.5	0.2	0.08
279/0.25/3.0/HighP	279	0.25	500	3.0	0.21	0.07
279/0.50/2.5/LowP	279	0.50	250	2.5	0.1	0.04
279/0.50/3.0/LowP	279	0.50	250	3.0	0.105	0.035
279/0.50/2.5/HighP	279	0.50	500	2.5	0.2	0.08

Table C.1 cont.

279/0.50/3.0/HighP	279	0.50	500	3.0	0.21	0.07
344/Flush/2.5/LowP	344	0	250	2.5	0.1	0.04
344/Flush/3.0/LowP	344	0	250	3.0	0.105	0.035
344/Flush/2.5/HighP	344	0	500	2.5	0.2	0.08
344/Flush/3.0/HighP	344	0	500	3.0	0.21	0.07
344/0.25/2.5/LowP	344	0.25	250	2.5	0.1	0.04
344/0.25/3.0/LowP	344	0.25	250	3.0	0.105	0.035
344/0.25/2.5/HighP	344	0.25	500	2.5	0.2	0.08
344/0.25/3.0/HighP	344	0.25	500	3.0	0.21	0.07
344/0.50/2.5/LowP	344	0.50	250	2.5	0.1	0.04
344/0.50/3.0/LowP	344	0.50	250	3.0	0.105	0.035
344/0.50/2.5/HighP	344	0.50	500	2.5	0.2	0.08
344/0.50/3.0/HighP	344	0.50	500	3.0	0.21	0.07

Table C.2 Swirl injectors test matrix

L^*, in	P_c, psia	O/F	$\dot{m}_{ox}$, lbm/s	$\dot{m}_f$, lbm/s
149	250	2.5	0.1	0.04
149	250	3.0	0.105	0.035
214	250	2.5	0.1	0.04
214	250	3.0	0.105	0.035
279	250	2.5	0.1	0.04
279	250	3.0	0.105	0.035
344	250	2.5	0.1	0.04
344	250	3.0	0.105	0.035

APPENDIX D

PLC Timing Control Diagrams

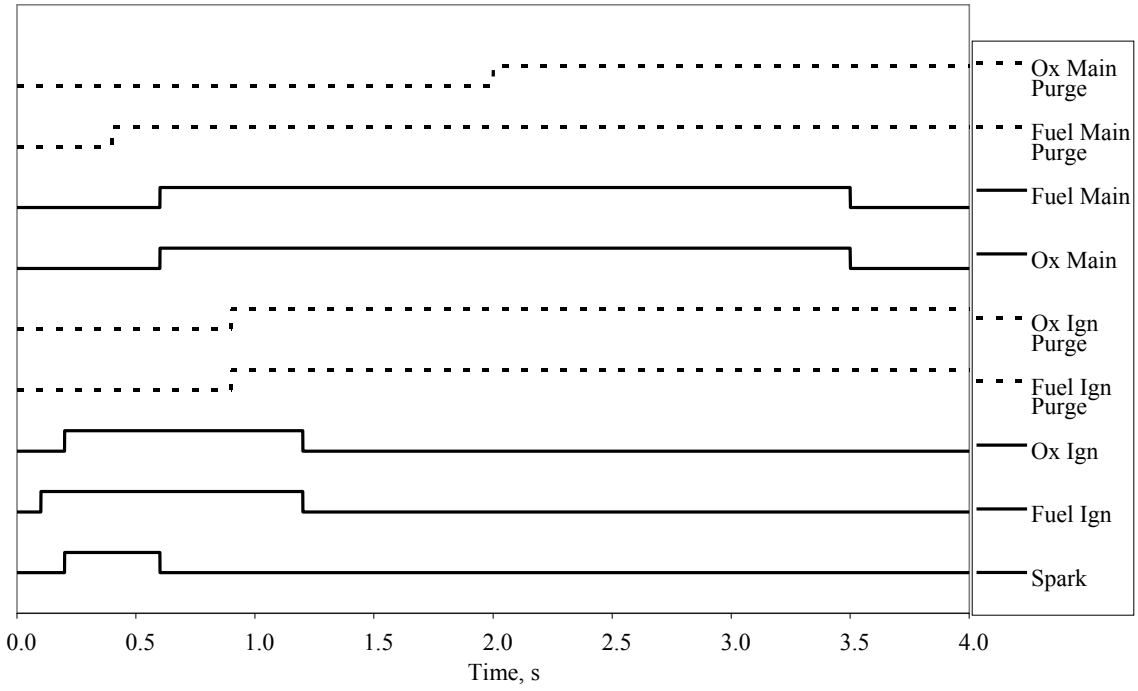

Figure D.1 PLC times for shear- and swirl coaxial injectors

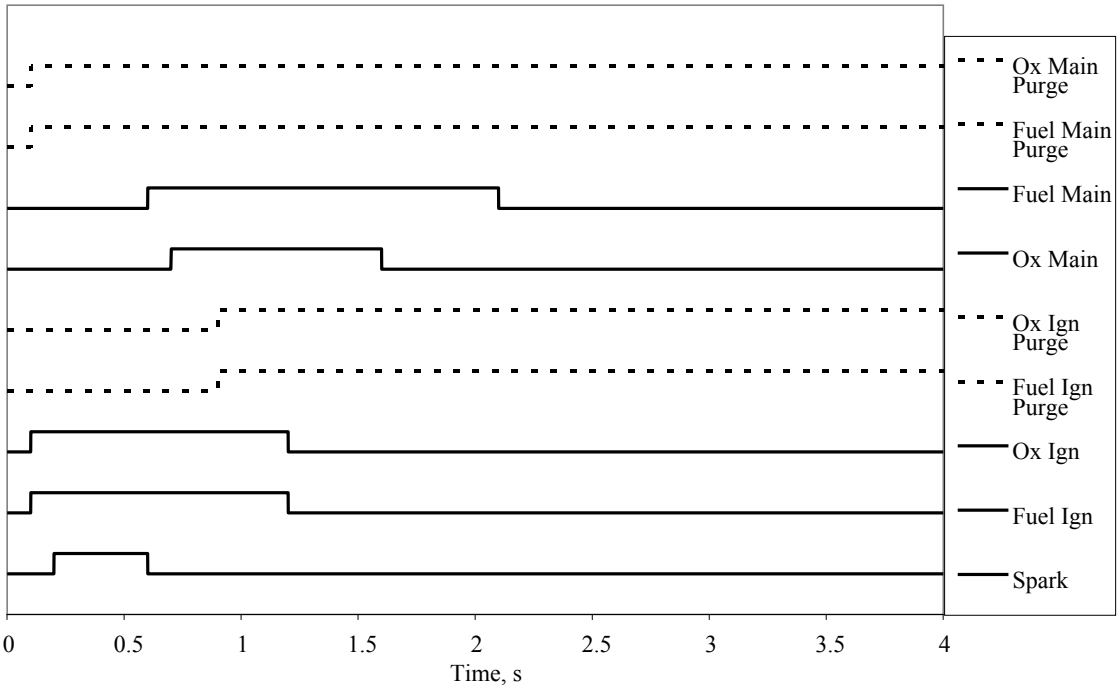

Figure D.2 PLC times for stainless steel and copper screw swirl injectors

APPENDIX E

Sensor Locations

Table E.1 Sensors used and tests locations

Sensor	Measurement	LabView Name	Test Stand	CH #
				BNC-2095 SC1Mod2
Sensotec1144528	Chamber	Pch	A1	1
Sensotec1196151	Igniter	P_Igniter	A2	0
Sensotec800528	Ox Injecter	P_Ox_Inj	A3	5
Sensotec768094	Fuel Injecter	P_Fuel_Inj	A7	7
Sensotec800523	Ox Venturi	P_Ox_Venturi	A6	6
Sensotec1196153	Fuel Venturi	P_Fuel_Venturi	A4	4
Setra1838940	Ox Ign Tank	P_Ox_Ign_Tank	B16	16
Senso740303	Ox Ign Dome	P_Ox_Ign_Dome	B9	17
Senso800732	Ox Ign Line	P_Ox_Ign_line	B14	18
Setra961950	Ox Ign Purge	P_Ox_Ign_Purge	B10	19
Setra1838938	Fuel Ign Tank	P_Fuel_Ign_Tank	A18	20
Senso642290	Fuel Ign Dome	P_Fuel_Ign_Dome	A13	21
Omega PX303A	Fuel Ign Line	P_Fuel_Ign_Line	B8	22
Setra1838937	Fuel Ign Purge	P_Fuel_Ign_Purge	A14	23
1232504	Ox Main Tank	P_Ox_Main_Tank	B15	24
Setra1838939	Ox Main Dome	P_Ox_Main_Dome	B11	25
Senso739772	Ox Main Purge	P_Ox_Main_Purge	B12	26
Senso800524	Fuel MainTank	P_Fuel_Main_Tank	A17	27
Setra2373105	Fuel Main Dome	P_Fuel_Main_Dome	A15	28
Setra1958693	Fuel Main Purge	P_Fuel_Main_Purge	A16	29
	Temperature			**TC-2095**
	Chamber	T Ch	K1	K1
	Igniter	T Ign	K2	K2
	Ox Venturi	T Ox	K3	K3
	Fuel Venturi	T Fuel	K4	K4

APPENDIX F

Swirl Coaxial Injector Calculations

$dP_{ox} := 70psi$ $dP_{fuel} := 70psi$ $P_c := 250psi$ $OF := 2.5$ $\alpha := 90deg$

$D_{n.ox} := .1in$ $D_{n.fuel} := .27in$ $L_{vc.ox} := .47in$ $L_{n.ox} := .1$ $Rbar_{in} := 1.2$

$D_{in.ox} := .06in$ $D_{in.fuel} := .08in$ $L_{vc.fuel} := .23in$ $L_{n.fuel} := .16in$ $Rbar_{ex} := 1$

$T := 300K$ $Ru := 8315\frac{J}{10^3 mol K}$ $MW_{ox} := 32\frac{kg}{10^3 mol}$ $MW_{fuel} := 16\frac{kg}{10^3 mol}$

$$\rho_{ox} := \frac{P_c}{\frac{Ru \cdot T}{MW_{ox}}} \qquad \rho_{ox} = 1.38\frac{lb}{ft^3} \qquad \rho_{fuel} := \frac{P_c}{\frac{Ru \cdot T}{MW_{fuel}}} \qquad \rho_{fuel} = 0.69\frac{lb}{ft^3}$$

$mdot_{tot} := .14\frac{lb}{s}$ $mdot_{ox} := .1\frac{lb}{s}$ $mdot_{fuel} := .04\frac{lb}{s}$

$$W_{\Sigma.ox} := \sqrt{\frac{2 \cdot dP_{ox}}{\rho_{ox}}} \qquad W_{\Sigma.ox} = 685.482\frac{ft}{s}$$

$$F_{jet.ox} := \frac{mdot_{ox}}{\rho_{ox} \cdot W_{\Sigma.ox}} \qquad F_{jet.ox} = 0.015in^2$$

$$D_{jet.ox} := \sqrt{\frac{4 \cdot F_{jet.ox}}{\pi}} \qquad D_{jet.ox} = 0.139in$$

$$a := \frac{\tan\left(\frac{\alpha}{2}\right)^2}{1 + \tan\left(\frac{\alpha}{2}\right)^2} \qquad a = 0.5$$

Given

$a = 0.5$ $\qquad \sqrt{a} = (1-\phi)\cdot\sqrt{\frac{2}{2-\phi}}$ $\qquad \phi := 0.3$

$\phi := \text{Find}(\phi)$ $\qquad \phi = 0.36$

Given

$\mu = \frac{\phi\cdot\sqrt{\phi}}{\sqrt{2-\phi}}$ $\qquad \phi = 0.36$ $\qquad \mu := 0.5$

$\mu := \text{Find}(\mu)$ $\qquad \mu = 0.168$

$A_{ox} := \frac{\sqrt{a}}{\mu}$ $\qquad A_{ox} = 4.2$

$F_{n.ox} := \frac{F_{jet.ox}}{\mu}$ $\qquad F_{n.ox} = 0.09\text{in}^2$

$R_{n.ox} := \sqrt{\frac{F_{n.ox}}{\pi}}$ $\qquad R_{n.ox} = 0.17\text{in}$

$D_{ox} := R_{n.ox}\cdot 2$ $\qquad D_{ox} = 0.339\text{in}$

$D_{ratio} := \frac{D_{ox}}{D_{n.ox}}$ $\qquad D_{ratio} = 3.392$

This implies that oxygen density is not correct.
Repeat calculations for cryogenic propellants.

$\rho_{ox} := 67.599\frac{\text{lb}}{\text{ft}^3}$ $\qquad \rho_{fuelstd} := 27.283\frac{\text{lb}}{\text{ft}^3}$

$mdot_{tot} := .14\frac{\text{lb}}{\text{s}}$ $\qquad mdot_{ox} := .1\frac{\text{lb}}{\text{s}}$ $\qquad mdot_{fuel} := .04\frac{\text{lb}}{\text{s}}$

$W_{\Sigma.ox} := \sqrt{\frac{2\cdot dP_{ox}}{\rho_{ox}}}$ $\qquad W_{\Sigma.ox} = 97.955\frac{\text{ft}}{\text{s}}$

$F_{jet.ox} := \frac{mdot_{ox}}{\rho_{ox}\cdot W_{\Sigma.ox}}$ $\qquad F_{jet.ox} = 2.175\times 10^{-3}\,\text{in}^2$

$D_{jet.ox} := \sqrt{\frac{4\cdot F_{jet.ox}}{\pi}}$ $\qquad D_{jet.ox} = 0.053\text{in}$

$$a := \frac{\tan\left(\frac{\alpha}{2}\right)^2}{1 + \tan\left(\frac{\alpha}{2}\right)^2} \qquad a = 0.5$$

Given

$a = 0.5$ $\qquad \sqrt{a} = (1 - \phi)\cdot\sqrt{\frac{2}{2 - \phi}}$ $\qquad \phi := 0.3$

$\phi := \text{Find}(\phi) \qquad \phi = 0.36$

Given

$\mu = \frac{\phi\cdot\sqrt{\phi}}{\sqrt{2 - \phi}}$ $\qquad \phi = 0.36$ $\qquad \mu := 0.5$

$\mu := \text{Find}(\mu) \qquad \mu = 0.168$

$A_{ox} := \frac{\sqrt{a}}{\mu} \qquad A_{ox} = 4.2$

$F_{n.ox} := \frac{F_{jet.ox}}{\mu} \qquad F_{n.ox} = 0.013\text{in}^2$

$R_{n.ox} := \sqrt{\frac{F_{n.ox}}{\pi}} \qquad R_{n.ox} = 0.064\text{in}$

$D_{ox} := R_{n.ox}\cdot 2 \qquad D_{ox} = 0.128\text{in}$

$D_{ratio} := \frac{D_{ox}}{D_{n.ox}} \qquad D_{ratio} = 1.282$

This shows that the designed oxygen swirl nozzle dimension is nearly the same as the physical dimension. This proves that this injector was originally designed for liquid propellants, not gaseous.

APPENDIX G

Operating Condition Calculations

$T_f := 540R$ $T_{ox} := 540R$ $Ru := 8315\frac{J}{10^3 \cdot mol \cdot K}$ $P_c := 250psi$

$\gamma_f := 1.305$ $\gamma_{ox} := 1.4$ $mdot_f := .04\frac{lb}{s}$ $mdot_{ox} := .1\frac{lb}{s}$

$MW_f := 16\frac{kg}{10^3 mol}$ $MW_{ox} := 32\frac{kg}{10^3 mol}$ $A_{inj.f} := .009864in^2$ $A_{inj.ox} := .047916in^2$

$$C_{star.f} := \frac{\sqrt{\gamma_f \frac{Ru \cdot T_f}{MW_f}}}{\gamma_f \sqrt{\left(\frac{2}{\gamma_f + 1}\right)^{\left(\frac{\gamma_f + 1}{\gamma_f - 1}\right)}}} \qquad C_{star.f} = 1.939 \times 10^3 \frac{ft}{s}$$

$$C_{star.ox} := \frac{\sqrt{\gamma_{ox} \frac{Ru \cdot T_{ox}}{MW_{ox}}}}{\gamma_{ox} \sqrt{\left(\frac{2}{\gamma_{ox} + 1}\right)^{\frac{\gamma_{ox} + 1}{\gamma_{ox} - 1}}}} \qquad C_{star.ox} = 1.338 \times 10^3 \frac{ft}{s}$$

$$D_{ven.f} := \sqrt{\frac{mdot_f \cdot C_{star.f} \cdot \frac{4}{\pi}}{P_c}} \qquad D_{ven.f} = 0.111in$$

$D_{vennf} := .093in$

$$D_{ven.ox} := \sqrt{\frac{mdot_{ox} \cdot C_{star.ox} \cdot \frac{4}{\pi}}{P_c}} \qquad D_{ven.ox} = 0.146in$$

$D_{vennox} := .113in$

$$P_{0.f} := \frac{C_{star.f} \cdot mdot_f}{\frac{\pi}{4} \cdot D_{ven.f}^2} \qquad P_{0.f} = 354.839psi$$

$$P_{0.ox} := \frac{C_{star.ox} \cdot mdot_{ox}}{\frac{\pi}{4} \cdot D_{ven.ox}^{2}}$$

$$P_{0.ox} = 414.6\,psi$$

$$\rho_f := P_c \cdot \frac{MW_f}{Ru \cdot T_f}$$

$$\rho_f = 0.69 \frac{lb}{ft^3}$$

$$\rho_{ox} := P_c \cdot \frac{MW_{ox}}{Ru \cdot T_{ox}}$$

$$\rho_{ox} = 1.38 \frac{lb}{ft^3}$$

$$v_f := \frac{mdot_f}{\rho_f A_{inj.f}}$$

$$v_f = 846.048 \frac{ft}{s}$$

$$v_{ox} := \frac{mdot_{ox}}{\rho_{ox} \cdot A_{inj.ox}}$$

$$v_{ox} = 217.709 \frac{ft}{s}$$

$$VR := \frac{v_f}{v_{ox}}$$

$$VR = 3.886$$

APPENDIX H

Uncertainty Calculations

Using $\eta_{C^*} = \dfrac{c^*_{act}}{c^*_{th}}$

Data Reduction Equation

$$\eta\left(P_c, P_{ox}, P_{fuel}, T_{ox}, T_{fuel}, D_t, D_{vo}, D_{vf}\right) := \frac{P_c \cdot \left(\frac{\pi}{4} \cdot D_t^{\,2}\right)}{\text{Denominator}}$$

$$\left[\frac{P_{ox} \cdot \left(\frac{\pi}{4} \cdot D_{vo}^{\,2}\right)}{\frac{\sqrt{\gamma_{ox} \frac{Ru}{MW_{ox}} \cdot T_{ox}}}{\gamma_{ox} \cdot \sqrt{\left(\frac{2}{\gamma_{ox}+1}\right)^{\frac{\gamma_{ox}+1}{\gamma_{ox}-1}}}}}\right] + \left[\frac{P_{fuel} \cdot \left(\frac{\pi}{4} \cdot D_{vf}^{\,2}\right)}{\frac{\sqrt{\gamma_{fuel} \frac{Ru}{MW_{fuel}} \cdot T_{fuel}}}{\gamma_{fuel} \cdot \sqrt{\left(\frac{2}{\gamma_{fuel}+1}\right)^{\frac{\gamma_{fuel}+1}{\gamma_{fuel}-1}}}}}\right]$$

$$\text{Denominator} := 210.96 \left[\frac{P_{ox} \cdot \left(\frac{\pi}{4} \cdot D_{vo}^{\,2}\right)}{\frac{\sqrt{\gamma_{ox} \frac{Ru}{MW_{ox}} \cdot T_{ox}}}{\gamma_{ox} \cdot \sqrt{\left(\frac{2}{\gamma_{ox}+1}\right)^{\frac{\gamma_{ox}+1}{\gamma_{ox}-1}}}}} \cdots\right]^3 - 2107.2 \left[\frac{P_{ox} \cdot \left(\frac{\pi}{4} \cdot D_{vo}^{\,2}\right)}{\frac{\sqrt{\gamma_{ox} \frac{Ru}{MW_{ox}} \cdot T_{ox}}}{\gamma_{ox} \cdot \sqrt{\left(\frac{2}{\gamma_{ox}+1}\right)^{\frac{\gamma_{ox}+1}{\gamma_{ox}-1}}}}} \cdots\right]^2 + \cdots$$

$$6731.2\left[\frac{P_{ox}\cdot\left(\frac{\pi}{4}\cdot D_{vo}^{\,2}\right)}{\sqrt{\gamma_{ox}\frac{Ru}{MW_{ox}}\cdot T_{ox}}\cdot\sqrt{\left(\frac{2}{\gamma_{ox}+1}\right)^{\frac{\gamma_{ox}+1}{\gamma_{ox}-1}}}}\cdot\frac{P_{fuel}\cdot\left(\frac{\pi}{4}\cdot D_{vf}^{\,2}\right)}{\sqrt{\gamma_{fuel}\frac{Ru}{MW_{fuel}}\cdot T_{fuel}}\cdot\sqrt{\left(\frac{2}{\gamma_{fuel}+1}\right)^{\frac{\gamma_{fuel}+1}{\gamma_{fuel}-1}}}}\right]-721.23-\left(\frac{500\cdot psi-P_c}{250\cdot psi}\right)\cdot..$$

$$\left[210.96\left[\frac{P_{ox}\cdot\left(\frac{\pi}{4}\cdot D_{vo}^{\,2}\right)}{\sqrt{\gamma_{ox}\frac{Ru}{MW_{ox}}\cdot T_{ox}}\cdot\sqrt{\left(\frac{2}{\gamma_{ox}+1}\right)^{\frac{\gamma_{ox}+1}{\gamma_{ox}-1}}}}\cdot\frac{P_{fuel}\cdot\left(\frac{\pi}{4}\cdot D_{vf}^{\,2}\right)}{\sqrt{\gamma_{fuel}\frac{Ru}{MW_{fuel}}\cdot T_{fuel}}\cdot\sqrt{\left(\frac{2}{\gamma_{fuel}+1}\right)^{\frac{\gamma_{fuel}+1}{\gamma_{fuel}-1}}}}\right]^3-2107.2\left[\frac{P_{ox}\cdot\left(\frac{\pi}{4}\cdot D_{vo}^{\,2}\right)}{\sqrt{\gamma_{ox}\frac{Ru}{MW_{ox}}\cdot T_{ox}}\cdot\sqrt{\left(\frac{2}{\gamma_{ox}+1}\right)^{\frac{\gamma_{ox}+1}{\gamma_{ox}-1}}}}\cdot\frac{P_{fuel}\cdot\left(\frac{\pi}{4}\cdot D_{vf}^{\,2}\right)}{\sqrt{\gamma_{fuel}\frac{Ru}{MW_{fuel}}\cdot T_{fuel}}\cdot\sqrt{\left(\frac{2}{\gamma_{fuel}+1}\right)^{\frac{\gamma_{fuel}+1}{\gamma_{fuel}-1}}}}\right]^2+..$$

$$6731.2\left[\frac{P_{ox}\cdot\left(\frac{\pi}{4}\cdot D_{vo}^{2}\right)}{\frac{\sqrt{\gamma_{ox}\cdot\frac{Ru}{MW_{ox}}\cdot T_{ox}}}{\gamma_{ox}\cdot\sqrt{\left(\frac{2}{\gamma_{ox}+1}\right)^{\frac{\gamma_{ox}+1}{\gamma_{ox}-1}}}}}\cdot\frac{P_{fuel}\cdot\left(\frac{\pi}{4}\cdot D_{vf}^{2}\right)}{\frac{\sqrt{\gamma_{fuel}\cdot\frac{Ru}{MW_{fuel}}\cdot T_{fuel}}}{\gamma_{fuel}\cdot\sqrt{\left(\frac{2}{\gamma_{fuel}+1}\right)^{\frac{\gamma_{fuel}+1}{\gamma_{fuel}-1}}}}}\right]-721.23-..$$

$$226.98\left[\frac{P_{ox}\cdot\left(\frac{\pi}{4}\cdot D_{vo}^{2}\right)}{\frac{\sqrt{\gamma_{ox}\cdot\frac{Ru}{MW_{ox}}\cdot T_{ox}}}{\gamma_{ox}\cdot\sqrt{\left(\frac{2}{\gamma_{ox}+1}\right)^{\frac{\gamma_{ox}+1}{\gamma_{ox}-1}}}}}\cdot\frac{P_{fuel}\cdot\left(\frac{\pi}{4}\cdot D_{vf}^{2}\right)}{\frac{\sqrt{\gamma_{fuel}\cdot\frac{Ru}{MW_{fuel}}\cdot T_{fuel}}}{\gamma_{fuel}\cdot\sqrt{\left(\frac{2}{\gamma_{fuel}+1}\right)^{\frac{\gamma_{fuel}+1}{\gamma_{fuel}-1}}}}}\right]^{3}-2215.4\left[\frac{P_{ox}\cdot\left(\frac{\pi}{4}\cdot D_{vo}^{2}\right)}{\frac{\sqrt{\gamma_{ox}\cdot\frac{Ru}{MW_{ox}}\cdot T_{ox}}}{\gamma_{ox}\cdot\sqrt{\left(\frac{2}{\gamma_{ox}+1}\right)^{\frac{\gamma_{ox}+1}{\gamma_{ox}-1}}}}}\cdot\frac{P_{fuel}\cdot\left(\frac{\pi}{4}\cdot D_{vf}^{2}\right)}{\frac{\sqrt{\gamma_{fuel}\cdot\frac{Ru}{MW_{fuel}}\cdot T_{fuel}}}{\gamma_{fuel}\cdot\sqrt{\left(\frac{2}{\gamma_{fuel}+1}\right)^{\frac{\gamma_{fuel}+1}{\gamma_{fuel}-1}}}}}\right]^{2}+..$$

$$6921.42\left[\frac{\frac{P_{ox}\cdot\left(\frac{\pi}{4}\cdot D_{vo}^{2}\right)}{\sqrt{\gamma_{ox}\cdot\frac{Ru}{MW_{ox}}\cdot T_{ox}}}}{\gamma_{ox}\cdot\sqrt{\left(\frac{2}{\gamma_{ox}+1}\right)^{\frac{\gamma_{ox}+1}{\gamma_{ox}-1}}}}-\frac{\frac{P_{fuel}\cdot\left(\frac{\pi}{4}\cdot D_{vf}^{2}\right)}{\sqrt{\gamma_{fuel}\cdot\frac{Ru}{MW_{fuel}}\cdot T_{fuel}}}}{\gamma_{fuel}\cdot\sqrt{\left(\frac{2}{\gamma_{fuel}+1}\right)^{\frac{\gamma_{fuel}+1}{\gamma_{fuel}-1}}}}\right]-795.6$$

Monte Carlo Uncertainty Analysis - 130/Flush/2.5/LowP Test

$n := 500$ number of iterations

$i := 1..n$ index variable

$D_t := .373\text{in}$ $D_{vo} := .113\text{in}$ $D_{vf} := .093\text{in}$

$A_t := \frac{\pi}{4}\cdot D_t^{\,2}$ $A_{vo} := \frac{\pi}{4}\cdot D_{vo}^{\,2}$ $Ru := 8315\frac{J}{mol\cdot K}$

$B_P := 3\text{psi}$ $A_{vf} := \frac{\pi}{4}\cdot D_{vf}^{\,2}$ $MW_{ox} := 32\frac{kg}{mol}$

$\gamma_{ox} := 1.4$ $\gamma_{fuel} := 1.3$ $MW_{fuel} := 16\frac{kg}{mol}$

Set Points

Systamatic and Random Uncertainty 95% confidence

$P_c := 178\text{psi}$

$P_{ox} := 390\text{psi}$ $U_{Pc} := \sqrt{B_P^{\,2} + \left(2\cdot\frac{1.395}{\sqrt{n}}\text{psi}\right)^2}$ $U_{Pc} = 3.003\text{psi}$

$P_{fuel} := 335\text{psi}$

$U_{Pox} := \sqrt{B_P^{\,2} + \left(2\cdot\frac{12.2}{\sqrt{n}}\text{psi}\right)^2}$ $U_{Pox} = 3.192\text{psi}$

$T_{ox} := 303\text{K}$

$T_{fuel} := 303.36\text{K}$ $U_{Pfuel} := \sqrt{B_P^{\,2} + \left(2\cdot\frac{0.069}{\sqrt{n}}\text{psi}\right)^2}$ $U_{Pfuel} = 3\text{ psi}$

$Pc := rnorm\left(n, \frac{P_c}{psi}, \frac{U_{Pc}}{2psi}\right)psi$ $U_{Tox} := \sqrt{(.0075\cdot T_{ox})^2 + \left(2\cdot\frac{.078}{\sqrt{n}}\text{K}\right)^2}$ $U_{Tox} = 2.273\text{K}$

$Pox := rnorm\left(n, \frac{P_{ox}}{psi}, \frac{U_{Pox}}{2psi}\right)psi$ $U_{Tfuel} := \sqrt{(.0075\cdot T_{fuel})^2 + \left(2\cdot\frac{.195}{\sqrt{n}}\cdot\text{K}\right)^2}$ $U_{Tfuel} = 2.275\text{K}$

$Pfuel := rnorm\left(n, \frac{P_{fuel}}{psi}, \frac{U_{Pfuel}}{2psi}\right)\cdot psi$ $U_{Dt} := .0005\text{in}$ $Dt := rnorm\left(n, \frac{D_t}{in}, \frac{U_{Dt}}{2in}\right)in$

$Tox := rnorm\left(n, \frac{T_{ox}}{K}, \frac{U_{Tox}}{2K}\right)\cdot K$ $U_{Dvo} := .0005\text{in}$ $Dvo := rnorm\left(n, \frac{D_{vo}}{in}, \frac{U_{Dvo}}{2in}\right)in$

$Tfuel := rnorm\left(n, \frac{T_{fuel}}{K}, \frac{U_{Tfuel}}{2K}\right)\cdot K$ $U_{Dvf} := .0005\text{in}$ $Dvf := rnorm\left(n, \frac{D_{vf}}{in}, \frac{U_{Dvf}}{2in}\right)in$

$$\eta_i := \eta\left(Pc_i, Pox_i, Pfuel_i, Tox_i, Tfuel_i, Dt_i, Dvo_i, Dvf_i\right)$$

$$\eta_{mean} := mean(\eta)$$

$$U_\eta := 2 \cdot stdev(\eta)$$

$\eta_{mean} = 76.993\%$ $U_\eta = 0.015$ This efficiency value matches original value

$$\frac{U_\eta}{\eta_{mean}} = 1.921\%$$

Monte Carlo Uncertainty Analysis - 325/Flush/2.5/HighP Test

$n := 500$ number of iterations

$i := 1..n$ index variable

$D_t := .373\text{in}$ $D_{vo} := .113\text{in}$ $D_{vf} := .093\text{in}$

$A_t := \frac{\pi}{4}\cdot D_t^{\,2}$ $A_{vo} := \frac{\pi}{4}\cdot D_{vo}^{\,2}$ $Ru := 8315\frac{J}{mol\cdot K}$

$B_P := 3\text{psi}$ $A_{vf} := \frac{\pi}{4}\cdot D_{vf}^{\,2}$ $MW_{ox} := 32\frac{kg}{mol}$

$\gamma_{ox} := 1.4$ $\gamma_{fuel} := 1.3$ $MW_{fuel} := 16\frac{kg}{mol}$

Set Points

$P_c := 444.8\text{psi}$

$P_{ox} := 795\text{psi}$

$P_{fuel} := 693.5\text{psi}$

$T_{ox} := 300\text{K}$

$T_{fuel} := 304.1\text{K}$

Systamatic and Random Uncertainty 95% confidence

$U_{Pc} := \sqrt{B_P^{\,2} + \left(2\cdot\frac{2.54}{\sqrt{n}}\text{psi}\right)^2}$ $U_{Pc} = 3.009\text{psi}$

$U_{Pox} := \sqrt{B_P^{\,2} + \left(2\cdot\frac{3.41}{\sqrt{n}}\text{psi}\right)^2}$ $U_{Pox} = 3.015\text{psi}$

$U_{Pfuel} := \sqrt{B_P^{\,2} + \left(2\cdot\frac{14.4}{\sqrt{n}}\text{psi}\right)^2}$ $U_{Pfuel} = 3.265\text{psi}$

$U_{Tox} := \sqrt{(.0075\,T_{ox})^2 + \left(2\cdot\frac{.078}{\sqrt{n}}\text{K}\right)^2}$ $U_{Tox} = 2.25\text{K}$

$U_{Tfuel} := \sqrt{(.0075\,T_{fuel})^2 + \left(2\cdot\frac{.195}{\sqrt{n}}\cdot\text{K}\right)^2}$ $U_{Tfuel} = 2.281\text{K}$

$Pc := rnorm\left(n, \frac{P_c}{psi}, \frac{U_{Pc}}{2psi}\right)\text{psi}$

$Pox := rnorm\left(n, \frac{P_{ox}}{psi}, \frac{U_{Pox}}{2psi}\right)\text{psi}$

$Pfuel := rnorm\left(n, \frac{P_{fuel}}{psi}, \frac{U_{Pfuel}}{2psi}\right)\cdot\text{psi}$

$Tox := rnorm\left(n, \frac{T_{ox}}{K}, \frac{U_{Tox}}{2K}\right)\cdot\text{K}$

$Tfuel := rnorm\left(n, \frac{T_{fuel}}{K}, \frac{U_{Tfuel}}{2K}\right)\cdot\text{K}$

$U_{Dt} := .0005\text{in}$ $Dt := rnorm\left(n, \frac{D_t}{in}, \frac{U_{Dt}}{2in}\right)\text{in}$

$U_{Dvo} := .0005\text{in}$ $Dvo := rnorm\left(n, \frac{D_{vo}}{in}, \frac{U_{Dvo}}{2in}\right)\text{in}$

$U_{Dvf} := .0005\text{in}$ $Dvf := rnorm\left(n, \frac{D_{vf}}{in}, \frac{U_{Dvf}}{2in}\right)\text{in}$

$$\eta_i := \eta\left(Pc_i, Pox_i, Pfuel_i, Tox_i, Tfuel_i, Dt_i, Dvo_i, Dvf_i\right)$$

$$\eta_{mean} := mean(\eta)$$

$$U_\eta := 2 \cdot stdev(\eta)$$

$\eta_{mean} = 93.342\%$ $U_\eta = 0.011$ This efficiency value matches original value

$$\frac{U_\eta}{\eta_{mean}} = 1.144\%$$

*L** Uncertainty

$D_C := 2.125in$ $D_t := .373in$ $R := \frac{2.125}{2}in$ $r := \frac{.373}{2}in$ $U_r := .005in$

$U_{DC} := .005in$ $U_{Dt} := .0005in$ $h := 1.5in$ $U_R := .005in$ $U_h := .005in$

$U_3 := .005in$ $U_1 := .005in$

$U_2 := .005in$

Individual uncertainties are based on machining tolerances of 0.005 in. or caliper measuring tolerance of 0.0005 in.

$$L := \begin{pmatrix} 4 \\ 6 \\ 8 \\ 10 \end{pmatrix} \text{in} \qquad RelU_{L.L} := \begin{bmatrix} \sqrt{\left(\frac{U_3}{3in}\right)^2 + \left(\frac{U_1}{1in}\right)^2} \\ \sqrt{\left(\frac{U_3}{3in}\right)^2 + \left(\frac{U_3}{3in}\right)^2} \\ \sqrt{\left(\frac{U_3}{3in}\right)^2 + \left(\frac{U_3}{3in}\right)^2 + \left(\frac{U_2}{2in}\right)^2} \\ \sqrt{\left(\frac{U_3}{3in}\right)^2 + \left(\frac{U_3}{3in}\right)^2 + \left(\frac{U_2}{2in}\right)^2 + \left(\frac{U_2}{2in}\right)^2} \end{bmatrix}$$

$$RelU_{L.L} = \begin{pmatrix} 0.527 \\ 0.236 \\ 0.344 \\ 0.425 \end{pmatrix} \%$$

Data Reduction Equation

$$Lstar := \frac{\frac{\pi}{4} \cdot D_C^{\,2} \cdot L + \pi \cdot \frac{h}{3} \cdot \left(R^2 + r \cdot R + r^2\right)}{\frac{\pi}{4} \cdot D_t^{\,2}} \qquad Lstar = \begin{pmatrix} 149.402 \\ 214.315 \\ 279.228 \\ 344.141 \end{pmatrix} \text{in}$$

Relative Uncertainty

$$dR := \frac{2 \cdot R + r}{\left(R^2 + R \cdot r + r^2\right)} \qquad dr := \frac{2 \cdot r + R}{R^2 + R \cdot r + r^2}$$

$$U_{Lstar.rel_0} := \sqrt{\left(\frac{2U_{DC}}{D_C}\right)^2 + \left(\frac{2U_{Dt}}{D_t}\right)^2 + \left(RelU_{L.L_0}\right)^2 + \left(dR \cdot U_R\right)^2 + \left(\frac{U_h}{h}\right)^2 + \left(dr \cdot U_r\right)^2}$$

$$U_{Lstar.rel_1} := \sqrt{\left(\frac{2U_{DC}}{D_C}\right)^2 + \left(\frac{2U_{Dt}}{D_t}\right)^2 + \left(RelU_{L.L_1}\right)^2 + \left(dR \cdot U_R\right)^2 + \left(\frac{U_h}{h}\right)^2 + \left(dr \cdot U_r\right)^2}$$

$$U_{Lstar.rel_2} := \sqrt{\left(\frac{2U_{DC}}{D_C}\right)^2 + \left(\frac{2U_{Dt}}{D_t}\right)^2 + \left(RelU_{L.L_2}\right)^2 + \left(dR \cdot U_R\right)^2 + \left(\frac{U_h}{h}\right)^2 + \left(dr \cdot U_r\right)^2}$$

$$U_{Lstar.rel_3} := \sqrt{\left(\frac{2U_{DC}}{D_C}\right)^2 + \left(\frac{2U_{Dt}}{D_t}\right)^2 + \left(RelU_{L.L_3}\right)^2 + \left(dR \cdot U_R\right)^2 + \left(\frac{U_h}{h}\right)^2 + \left(dr \cdot U_r\right)^2}$$

$U_{Lstar.rel_0} = 1.296\%$ $\qquad$ $U_{Lstar.rel_2} = 1.233\%$

$U_{Lstar.rel_1} = 1.207\%$ $\qquad$ $U_{Lstar.rel_3} = 1.258\%$

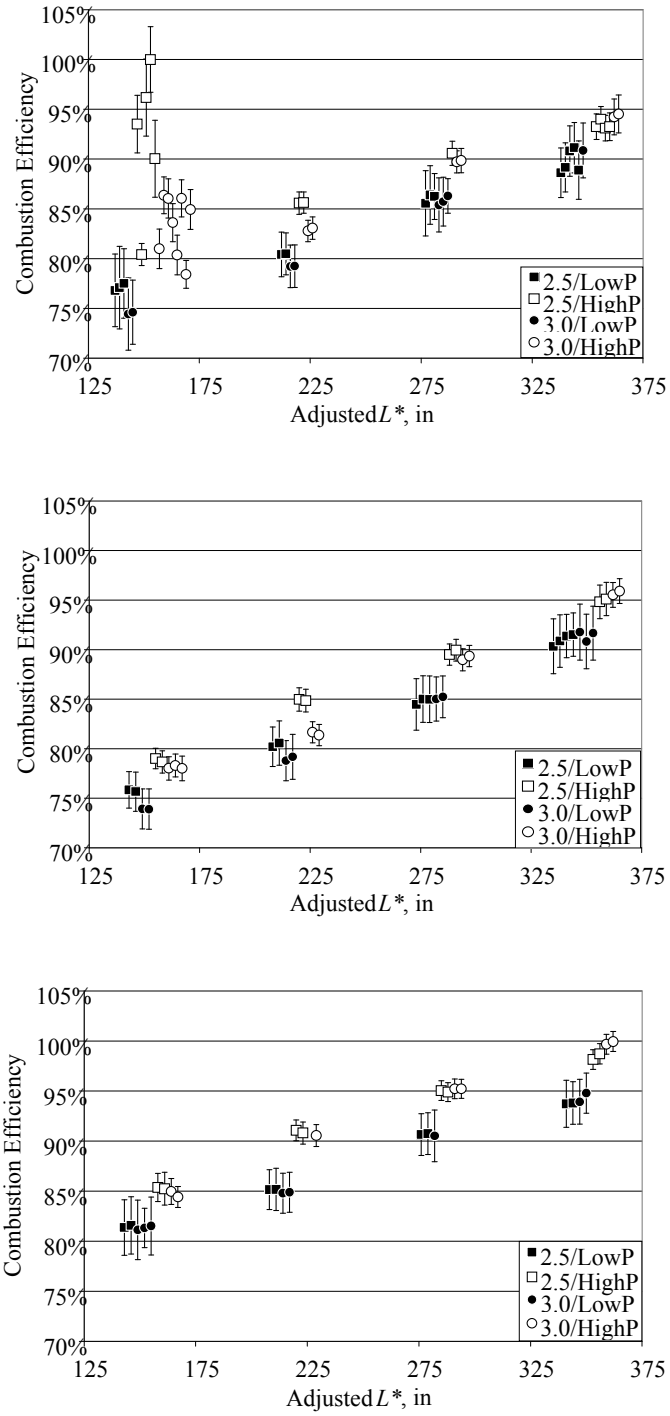

Figure H.1 Shear coaxial hot-fire results with uncertainty bars.
[L^* values have been adjusted around the nominal value to distinguish between data points. a) Flush oxygen post; b) 0.25 inch recess; c) 0.50 inch recess]

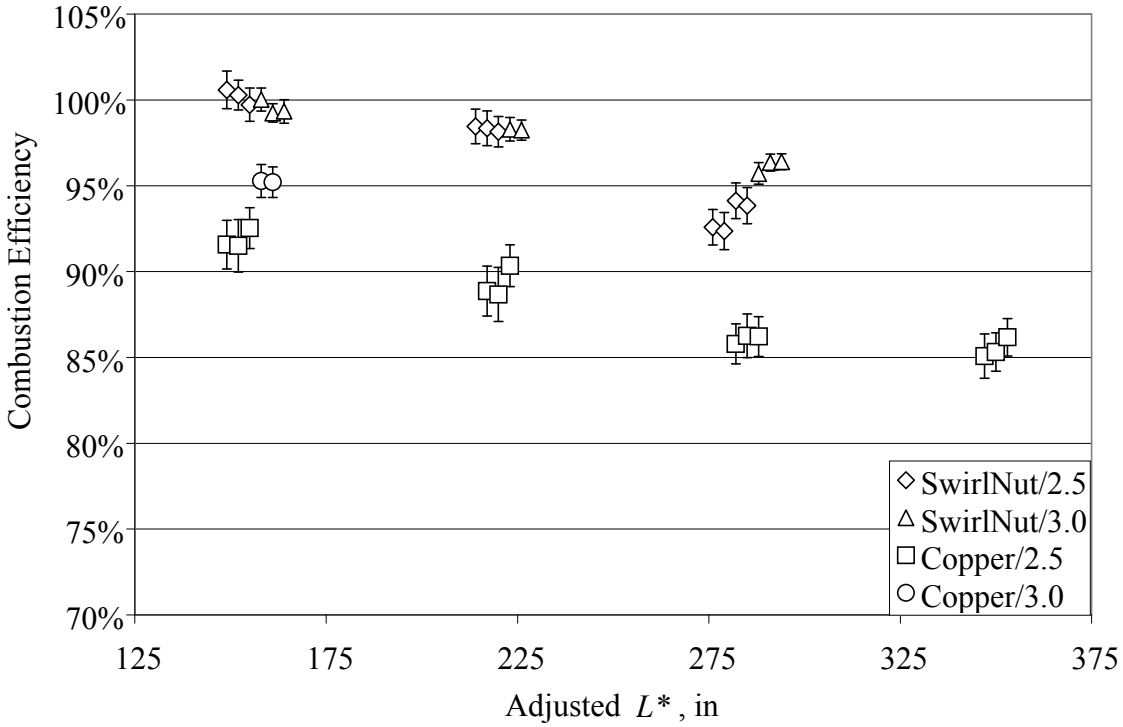

Figure H.2 Results of swirl injectors with uncertainty bars.
[L^* values have been adjusted around nominal value to distinguish between data points]

REFERENCES

[1]Turns, S., *An Introduction to Combustion, Concepts and Applications*, 2nd ed., McGraw-Hill, Boston, 2000.

[2]Zong, N., and Yang, V., "A Numerical Study of High-Pressure Oxygen/Methane Mixing and Combustion of a Shear Coaxial Injector," AIAA 2005-152, 43rd AIAA Aerospace Science Meeting and Exhibit, Reno, NV, January 10-13, 2005.

[3]Zong, N., and Yang, V., "Supercritical LOX/Methane Flame Stabilization and Dynamics of a Shear Coaxial Injector," AIAA 2006-760, 44th AIAA Aerospace Science Meeting and Exhibit, Reno, NV, January 9-12, 2006.

[4]Gill, G. S., and Nurick, W. H., "Liquid Rocket Engine Injectors," NASA SP-8089, March 1976.

[5]Bazarov, V., "Survey and Classification of Injectors used in LPRE," UAH Report, 2008.

[6]Sasaki, M., Sakamoto, H., Takahashi, M., Tomita, T., and Tamura, H., "Experimental Study on Combustion Stability Characteristics of Non-Swirl and Swirl Coaxial Injectors," AIAA 98-3438, 34th AIAA/ASME/SAE/ASEE Joint Propulsion Conference and Exhibit, Cleveland, OH, July 13-15, 1998.

[7]Hulka, J., and Makel, D., "Liquid Oxygen/Hydrogen Testing of a Single Swirl Coaxial Injector Element in a Windowed Combustion Chamber," AIAA 93-1954, AIAA/SAE/ASME/ASEE 29th Joint Propulsion Conference and Exhibit, Monterey, CA, June 28-30, 1993.

[8]Kalitan, D. M., Salgues, D., Mouis, A. G., Lee, S. Y., Pal, S., and Santoro, R. J., "Experimental Liquid Rocket Swirl Coaxial Injector Study Using Non-Intrusive Optical Techniques," AIAA 2005-4299, 41st AIAA/ASME/SAE/ASEE Joint Propulsion Conference and Exhibit, Tucson, AZ, July 10-13, 2005.

[9]Bayvel, L., and Orzhechovski, Z., *Liquid Atomization*, Taylor and Francis, 1993.

[10]Long, M., Bazarov, V., and Anderson, W., "Main Chamber Injectors for Advanced Hydrocarbon Booster Engines," AIAA 2003-4599, 39th AIAA/ASME/SAE/ASEE Joint Propulsion Conference and Exhibit, Huntsville, AL, July 20-23, 2003.

[11]Parish, J. R. Jr., "Fuel Injector Having an Internally Mounted Cross-Flow Nozzle for Enhanced Compressed Natural Gas Jet Spray," Pub. No. WO/2008/005491, October 2008.

[12]Sutton, G., and Biblarz, O., *Rocket Propulsion Elements*, 7th edition, Wiley-Interscience, 2000.

[13]Calhoon, D. F., Ito, J. I., and Kors, D. L., "Investigation of Gaseous Propellant Combustion and Associated Injector/Chamber Design Guidelines," NASA CR-121234, July 1973.

[14]Rupe, J. H., "A Correlation Between the Dynamic Properties of a Pair of Impinging Streams and the Uniformity of Mixing Ratio Distribution in the Resulting Spray," Progress Report No. 20-209, Jet Propulsion Laboratory, Pasadena, CA, March 1956.

[15]Sutton, G. P., *History of Liquid Propellant Rocket Engines*, AIAA *Library of Flight Series*, 2006.

[16]Yang, V., Habiballah, M., Hulka, J., and Popp, M., *Liquid Rocket Thrust Chambers: Aspects of Modeling, Analysis, and Design*, Vol. 200, Progress in Astronautics and Aeronautics, AIAA, 2004, pp. 19-103.

[17]"Hydrogen-Oxygen Auxiliary Propulsion for the Space Shuttle – Volume 1: High Pressure Thrusters," NASA CR-120895, January 1973.

[18]Cavitt, R., *Experimental Methodology for Measuring Combustion and Injection Coupled Responses*, UAHuntsville Master's Thesis, Huntsville, AL, 2007.

[19]Ferraro, M., Kujala, R. J., Thomas, J. L., Glogowski, M. J., and Micci, M. M., "Effects of GH_2/LOX Velocity and Momentum Ratios on Shear Coaxial Injector Atomization," *Journal of Propulsion and Power*, Vol. 18, No. 1, 2001, pp. 209-211.

[20]Beisler, M. A., Pal, S., Moser, M. D., and Santoro, R. J., "Shear Coaxial Injector Atomization in a LOX/GH_2 Propellant Rocket," AIAA 94-2775, AIAA/ASME/SAE/ASEE 29th Joint Propulsion Conference and Exhibit, Indianapolis, IN, June 27-29, 1994.

[21]Haeseler, D., Roubinski, V., Khrissanfov, S., and Berejnoy, V., "Testing of LOX-Hydrocarbon Thrust Chambers for Future Reusable Launch Vehicles," AIAA 2002-3845, 38th AIAA/ASME/SAE/ASEE Joint Propulsion Conference and Exhibit, Indianapolis, IN, 7-10 July, 2002.

[22]Cho, Y. H., and Chang, H. S., "Hot Firing Tests of Liquid Rocket Engine Using LOX/LNG," AIAA 2004-3528, 40th AIAA/SAE/ASME/ASEE Joint Propulsion Conference and Exhibit, Fort Lauderdale, FL, 11-14 July, 2004.

[23]Singla, G., Scouflaire, P., Rolon, C., and Candel, S., "Transcritical Oxygen/Transcritical or Supercritical Methane Combustion," *Proceedings of the Combustion Institute*, Vol. 30, 2005, pp. 2921-2928.

[24]Tamura, H., Sakamoto, H., Sasaki, M., Takahashi, M., Tomita, T., and Mayer, W., "An Experimental Study on the Stability Characteristics of the LOX/Methane Rocket Combustor," AIAA 95-2359, 31st AIAA/ASME/SAE/ASEE Joint Propulsion Conference and Exhibit, San Diego, CA, July 10-12, 1995.

[25]Bazarov, V., Rutovskii, V., and Khohlov, A., "Study of Atomization, Mixing, and Combustion of Liquid and Gaseous Propellants in Crossed and Swirled Flows," AIAA 2007-5684, 43rd AIAA/ASME/SAE/ASEE Joint Propulsion Conference and Exhibit, Cincinnati, OH, July 8-11, 2007.

[26]Hulka, J., and Schneider, J. A., "Single Element Injector Cold Flow Testing for STME Swirl Coaxial Injector Element Design," AIAA 93-2161, 29th AIAA/SAE/ASME/ASEE Joint Propulsion Conference and Exhibit, Monterey, CA, June 28-30, 1993.

[27]Zong, N., and Yang, V., "Near-Field Flow and Flame Dynamics of LOX/Methane Shear Coaxial Injector Under Supercritical Conditions," Proceedings of the Combustion Institute, Vol. 31, 2007, pp. 2309-2317.

[28]Zurbach, S., Thomas, J. L., Vuillermoz, P., Vingert, L., and Habiballah, M., "Recent Advances on LOX/Methane Combustion for Liquid Rocket Engine Injector," AIAA 2002-4321, 38th AIAA/SAE/ASME/ASEE Joint Propulsion Conference and Exhibit, Indianapolis, IN, July 7-10, 2002.

[29]Pal, S., Moser, M. D., Ryan, H. M., Foust, M. J., and Santoro, R. J., "Flowfield Characteristics in a Liquid Propellant Rocket," AIAA 93-1882, AIAA/SAE/ASME/ASEE 29th Joint Propulsion Conference and Exhibit, Monterey, CA, June 28-30, 1993.

[30]Moser, M. D., Merenich, J. J., Pal, S., and Santoro, R. J., "OH-Radical Imaging and Velocity Field Measurements in a Gaseous Hydrogen/Oxygen Rocket," AIAA 93-2036, AIAA/SAE/ASME/ASEE 29th Joint Propulsion Conference and Exhibit, Monterey, CA, June 28-30, 1993.

[31]Singla, G., Scouflaire, P., Rolon, C., and Candel, S., "Transcritical Oxygen/Transcritical or Supercritical Methane Combustion," *Proceedings of the Combustion Institute*, Vol. 30, 2005, pp. 2921-2928.

[32]Salgues, D., Mouis, A.-G., Lee, S.-Y., Kalitan, D., Pal, S., and Santoro, R., "Shear and Swirl Coaxial Injector Studies of LOX/GCH_4 Rocket Combustion using Non-Intrusive Laser Diagnostics," AIAA 2006-757, 44th AIAA Aerospace Sciences Meeting and Exhibit, Reno, NV, January 9-12, 2006.

[33]Lux, J., Suslov, D., and Haidn, O., "On Porous Liquid Propellant Rocket Engine Injectors," *Aerospace Science and Technology*, Vol. 11, No. 1, 2007, In Press.

[34]Kaltz, T., Milicic, M., Glogowski, M., and Micci, M. M., "Shear Coaxial Injector Spray Characterization," AIAA 93-2190, AIAA/SAE/ASME/ASEE 29th Joint Propulsion Conference and Exhibit, Monterey, CA, June 28-30, 1993.

[35]Rahman, S. A., Pal, S., and Santoro, R. J., "Swirl Coaxial Atomization: Cold-Flow and Hot-Fire Experiments," AIAA 95-0381, 33rd Aerospace Sciences Meeting and Exhibit, Reno, NV, January 9-12, 1995.

[36]Trinh, H. P., "Liquid Methane/Oxygen Injector Study for Potential Future Mars Ascent Engines," AIAA 2000-3119, 36th AIAA/ASME/SAE/ASEE Joint Propulsion Conference and Exhibit, Huntsville, AL, 17-19 July, 2000.

[37]Yatsuyanagi, N., Gomi, H., Sakamoto, H., and Narasaki, T., "An Empirical Expression of the C* Efficiency of LO_2/Hydrogen Rocket Combustor with Coaxial Injector," AIAA 85-1387, AIAA/SAE/ASME/ASEE 21st Joint Propulsion Conference, Monterey, CA, July 8-10, 1985.

[38]Tamura, H., Ono, F., Kumakawa, A., and Yatsuyanagi, N., "LOX/Methane Staged Combustion Rocket Combustor Investigation," AIAA 87-1856, AIAA/SAE/ASME/ASEE 23rd Joint Propulsion Conference, San Diego, CA, June 29 – July 2, 1987.

[39]TEP, Thermal Equilibrium Program, Software Package, Ver. 1.0, Software and Engineering Associates, Inc., Carson City, NV, 2002.

[40]Woodward, R. D., Pal, S., Farhangi, S., Jensen, G. E., and Santoro, R. J., "LOX/GH_2 Shear Coaxial Injector Atomization Studies: Effect of Recess and Non-Concentricity," AIAA 2007-571, 45th AIAA Aerospace Sciences Meeting and Exhibit, Reno, NV, January 8-11, 2007.

[41]Yang, V., and Anderson, W., *Liquid Rocket Engine Combustion Instability*, Vol. 169, Progress in Astronautics and Aeronautics, AIAA, 1995, pp. 39-71.

[42]Ellison, L. R., and Moser, M. D., "Combustion Instability Analysis and the Effects of Drop Size on Acoustic Driving Rocket Flow," NASA NCC8-200, 2005.

[43]Tamura, H., Sakamoto, H., Takahashi, M., Sasaki, M., Tomita, T., and Nagao, R., "LOX/LH_2 Subscale Swirl Coaxial Injector Testing," AIAA 97-2906, 33rd AIAA/ASME/SAE/ASEE Joint Propulsion Conference and Exhibit, Seattle, WA, July 6-9, 1997.

[44]Johnson, R. J., "Hydrogen-Oxygen Catalytic Ignition and Thruster Investigation – Volume 1: Catalytic Ignition and Low Pressure Thruster Evaluations," NASA CR-120869, November 1972.